Report on tuner design

Paolo Pierini, Nicola Panzeri,
Angelo Bosotti, Paolo Michelato, Carlo Pagani, Rocco Paparella

INFN Sezione di Milano - LASA

Abstract

We document here the coaxial ("blade") tuner design for TRASCO Cavity A of the HIPPI program, which is entering fabrication stage. We first document the full RF and mechanical characterization of the structure, and the interpretation of the cavity tests at Saclay and Jefferson Lab, in order to specify the tuner requirements.
The purpose of this document is also to collect in a single place the cavity system (structure + tuner) characterization, both from the RF and mechanical point of views, in order to allow for the cavity (A and B) comparison activities at the end of the HIPPI program.

Report on tuner design

Paolo Pierini, Nicola Panzeri,
Angelo Bosotti, Paolo Michelato, Carlo Pagani, Rocco Paparella
INFN Milano LASA

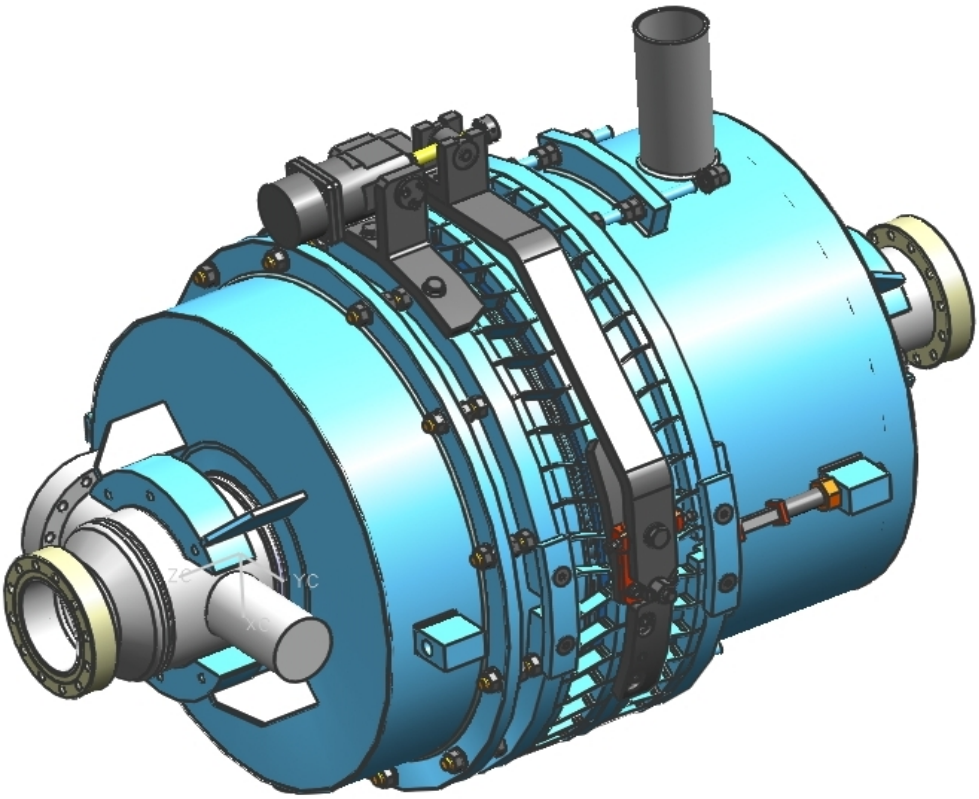

Document date: 22 March 2006

Table of Contents

List of Tables

List of Figures

1 Introduction

In this note we describe the design of the coaxial “blade” tuner with slow and fast tuning capabilities for the TRASCO Z501/Z502 cavities (Cavity A in HIPPI) developed at INFN Milano for the HIPPI program.

In order to finalize the tuner design, the cavity has been fully characterized in terms of electromagnetic and mechanical performance. RF and mechanical models of the cavity have been developed and coupled together in order to determine the frequency offset under a variety of mechanical load conditions.

Paragraph 2 reports the characterization of the RF structure itself – and the model used for the frequency shift evaluation through the Slater perturbation theorem - while Paragraph 3, 4 and 5 deal with the other three main mechanical components that play a major role in the mechanical and frequency behavior of the “dressed” cavity: the He tank supports (end dishes), the He tank and the tuner mechanism itself.

Paragraph 6 is dedicated to the axial and bending behavior of the complete system (the “dressed” cavity, consisting of the structure, the He tank and tuner system).

Paragraph 7 is dedicated to the estimation of the static Lorentz Force Detuning coefficient under arbitrary boundary conditions, and Paragraph 8 reports the full understanding of the LFD measurements obtained during the RF tests performed at Saclay and JLAB.

Paragraph 9 lists the cavity mechanical eigenmodes of the bare cavity.

Paragraph 10 summarizes the cavity/tuner characterization in terms of the HIPPI requirements.

The present note is intended to report exhaustively on all the modeling activities performed on Cavity A and the associated cold tuner mechanism, in order to facilitate the RF structure comparison activities planned before the end of the HIPPI program.

2 Electromagnetic and mechanical characterization of the TRASCO cavity

2.1 Geometry

The design of the TRASCO cavity, its physical dimensions and the results of the vertical RF tests, have been extensively reported in a dedicated HIPPI Note [1], as well as reported in several papers at conferences [2]. The RF tests of single cell prototypes and multicell structures have been reported in [3] and [4].

2.2 RF Characterization

In the following we provide the geometry description for the Superfish analysis of the cavity, and the code outputs (normalized to an accelerating field of 1 MV/m).

2.2.1 Superfish input

```
SuperFish File generated from BuildCav 1.3.4
$reg kprob=1,
 freq=704.438
 xdri=42., ydri=18.6041
 nbslf=1,nbsrt=1,
 beta=0.47, rmass = -2, kmethod=1, dphi=180,
 irtype=1, tempk=2.0, tc=9.2, residr=0.0,
 clength=50.  zctr=42. norm=1
 dx=,
 xreg=16,18,26,28,36,38,46,48,56,58,66,68
 kreg=0,80,130,210,260,340,390,470,520,600,650,730,780,
 kmax=875
 yreg=3,5,10
 lreg=0,31,131,180,
 lmax=200$

$po x=0,y=0$
$po x=0, y=4. $
$po x=17., y=4. $
$po nt=2, x0=17., y0=5.043, A=0.8023, B=1.043, x=0.7949, y=-0.1414$
$po x=18.7632, y=14.0988$
$po nt=2, x0=22, y0=13.114, A=3.2883, B=5.59, x=0.0, y=5.59$
$po nt=2, x0=22., y0=13.324, A=3.3625, B=5.38, x=3.3233, y=0.8192$
$po x=26.2131, y=4.903$
$po nt=2, x0=27. y0=5.031, A=0.7931, B=1.031, x=0, y=-1.031$
$po nt=2, x0=27., y0=5.031, A=0.7931, B=1.031, x=0.7869, y=-0.1281$
$po x=28.6767, y=14.1432$
$po nt=2, x0=32, y0=13.324, A=3.3625, B=5.38, x=0.0, y=5.38$
$po nt=2, x0=32., y0=13.324, A=3.3625, B=5.38, x=3.3233, y=0.8192$
$po x=36.2131, y=4.903$
$po nt=2, x0=37. y0=5.031, A=0.7931, B=1.031, x=0, y=-1.031$
$po nt=2, x0=37., y0=5.031, A=0.7931, B=1.031, x=0.7869, y=-0.1281$
$po x=38.6767, y=14.1432$
$po nt=2, x0=42, y0=13.324, A=3.3625, B=5.38, x=0.0, y=5.38$
$po nt=2, x0=42., y0=13.324, A=3.3625, B=5.38, x=3.3233, y=0.8192$
$po x=46.2131, y=4.903$
$po nt=2, x0=47. y0=5.031, A=0.7931, B=1.031, x=0, y=-1.031$
$po nt=2, x0=47., y0=5.031, A=0.7931, B=1.031, x=0.7869, y=-0.1281$
$po x=48.6767, y=14.1432$
$po nt=2, x0=52, y0=13.324, A=3.3625, B=5.38, x=0.0, y=5.38$
$po nt=2, x0=52., y0=13.324, A=3.3625, B=5.38, x=3.3233, y=0.8192$
$po x=56.2131, y=4.903$
$po nt=2, x0=57. y0=5.031, A=0.7931, B=1.031, x=0, y=-1.031$
$po nt=2, x0=57., y0=5.031, A=0.7931, B=1.031, x=0.7869, y=-0.1281$
$po x=58.6767, y=14.1432$
$po nt=2, x0=62, y0=13.324, A=3.3625, B=5.38, x=0.0, y=5.38$
```

```
$po nt=2, x0=62., y0=15.0446, A=3.6595, B=3.6595, x=3.6463, y=0.3104$
$po x=66.334, y=7.2753$
$po nt=2, x0=67. y0=7.3711, A=0.6701, B=0.8711, x=0, y=-0.8711$
$po x=82., y=6.5 $
$po x=84.5, y=4. $
$po x=87., y=4. $
$po x=87., y=0 $
$po x=0,y=0$
```

2.2.2 Graphical output of RF calculations

The computed frequency from the above input file=704.477 MHz.

2.2.2.1 Field pattern

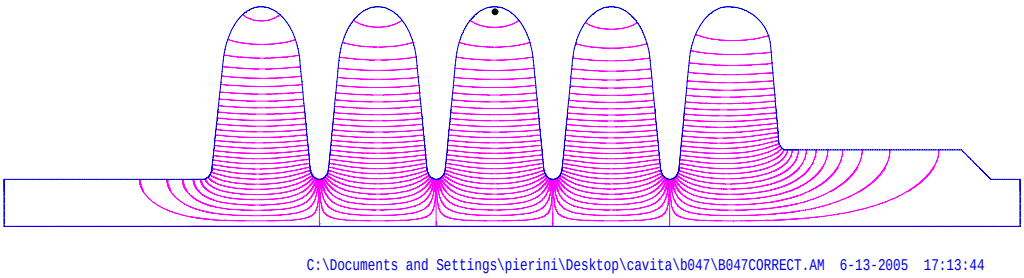

Figure 1: The electric field lines from Superfish.

2.2.2.2 Field Flatness

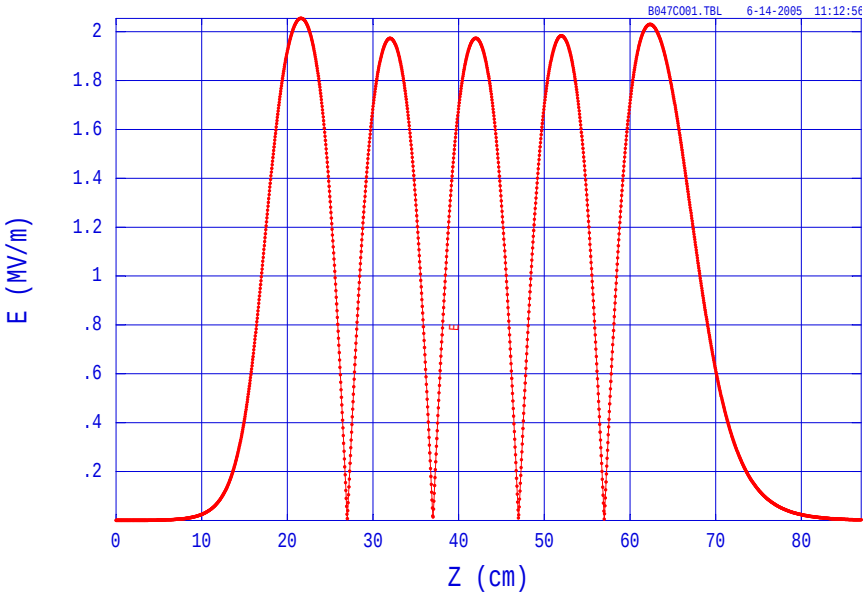

Figure 2: The absolute value of the on-axis field.

2.2.3 RF output parameters (SFO)

```
All calculated values below refer to the mesh geometry only.
Field normalization (NORM = 1):    EZEROT =      1.00000 MV/m
Length used for E0 normalization          =     50.00000 cm
Frequency                                 =    704.47797 MHz
Particle rest mass energy                 =   938.272029 MeV
Beta =  0.4700000          Kinetic energy =      124.725 MeV
Normalization factor for E0 =  1.558 MV/m =    15962.540
Transit-time factor                       =    0.6420298
Stored energy                             =    0.3558708 Joules
Superconductor surface resistance         =       4.9324 nanoOhm
Operating temperature                     =       2.0000 K
Power dissipation                         =      51.9715 mW
```

```
Q    =    3.0309E+10      Shunt impedance =   2.3340E+07 MOhm/m
Rs*Q =   149.496 Ohm                Z*T*T =   9.6207E+06 MOhm/m
r/Q  =   158.709 Ohm  Wake loss parameter =      0.17563 V/pC
Average magnetic field on the outer wall  =      4187.87 A/m, 4.32527 uW/cm^2
Maximum H (at Z,R = 65.7249,14.4315)      =      4775.79 A/m, 5.62493 uW/cm^2
Maximum E (at Z,R = 66.4776,6.82557)      =      3.60617 MV/m, 0.146532 Kilp.
Ratio of peak fields Bmax/Emax            =       1.6642 mT/(MV/m)
Peak-to-average ratio Emax/E0             =       2.3153
```

2.3 Frequency displacement calculation methodology

We summarize here the method used for the frequency displacement evaluation using different mechanical loads on the structure. The latest versions of Superfish allow to extract geometrical information on the metallic cavity walls, as well as the equivalent mechanical pressure associated to the electromagnetic fields in the cavity needed for Lorentz force detuning calculation. The geometry displacement calculated with a mechanical code (in our case ANSYS) can then be loaded by one of Superfish preprocessors (Automesh) in order to perturb the geometrical boundary of the cavity. The resonant frequency is then evaluated on the new meshing, where only the boundary is perturbed. We have extensively used this feature of the Supefish code while debugging a fully independent Slater perturbation procedure.
The perturbation procedure, including the geometrical model used to evaluate the infinitesimal volume change at each boundary position due to the cavity wall displacement is documented here.

2.3.1 Slater perturbation method

If the cavity, with an energy content U and an initial frequency ν, is perturbed in its geometrical boundary over a small volume δV, the resulting frequency perturbation is, according to Slater theorem [5]:

$$\frac{\Delta\nu}{\nu} = \frac{1}{4U}\int_{\delta V} dV\left(\varepsilon_0 E^2 - \mu_0 H^2\right)$$

where the integral is performed over the change in the cavity boundary. The electric and magnetic fields are usually provided by an RF eigenmode solver program (like Superfish), whereas the infinitesimal volume change needs to be evaluated from the mechanical displacements induced on the cavity.

2.3.1.1 Electromagnetic pressure load case (LFD)

The electromagnetic field in the cavity itself exerts a pressure on the cavity walls. In the standing wave case, and averaging over the rapid temporal variation of the fields at the nominal frequency, [5] the pressure load is given by:

$$P_{sw} = \frac{1}{4}\left(\mu_0 H^2 - \varepsilon_0 E^2\right)$$

2.3.1.2 Problem discretization

The unperturbed geometry is stored in two arrays: Z (coordinate along the beam axis) and R (radial coordinate), whereas the geometry displacements (calculated via a structural ANSYS model) are stored in the arrays uz and ur. The fields at the given positions are stored in the arrays E and H. The pressure load and the Slater coefficients can thus be stored in the arrays P and df^{Slater}, defined below.

$$P_j = \frac{1}{4}\left(\mu_0 H_j^2 - \varepsilon_0 E_j^2\right) \qquad j = 1,...nz$$

$$df_j^{Slater} = \frac{1}{4}\left(\varepsilon_0 E_j^2 - \mu_0 H_j^2\right) = -P_j \qquad j = 1,...nz$$

2.3.1.3 Infinitesimal frequency change

With the discretization discussed above, the infinitesimal frequency change $\Delta\nu_j$ for a small perturbation volume dV_j around the j^{th} point at Z_j, R_j is given by:

$$\Delta\nu_j = \frac{\nu}{U} df_j^{Slater} dV_j$$

The total frequency change can then be evaluated summing over the elements of the $\Delta\nu$ vector.

2.3.1.4 Evaluation of the infinitesimal volume change

The problem has then been reduced to the evaluation of the infinitesimal volume change dV_j due to the displacement vector (uz_j,ur_j). The sketch of the situation for an internal point of the boundary consisting of nz points is illustrated in the next figure.
In the figure labels we have used the following notation:

$L_j = \sqrt{(Z_{j+1} - Z_j)^2 + (R_{j+1} - R_j)^2}$	Distance between mesh points j and $j+1$
$us_j = \sqrt{uz_j^{\,2} + ur_j^{\,2}}$	Lenght of the displacement vector
$\theta_j = Tan^{-1}\dfrac{R_j - R_{j+1}}{Z_{j+1} - Z_j}$	Mesh inclination
$\phi_j = Tan^{-1}\dfrac{ur_j}{uz_j}$	Displacement inclination
$\alpha_j^+ = \phi_j + \theta_j$	Angle for right area calculation
$\alpha_j^- = \pi - \phi_j - \theta_{j-1}$	Angle for left area calculation

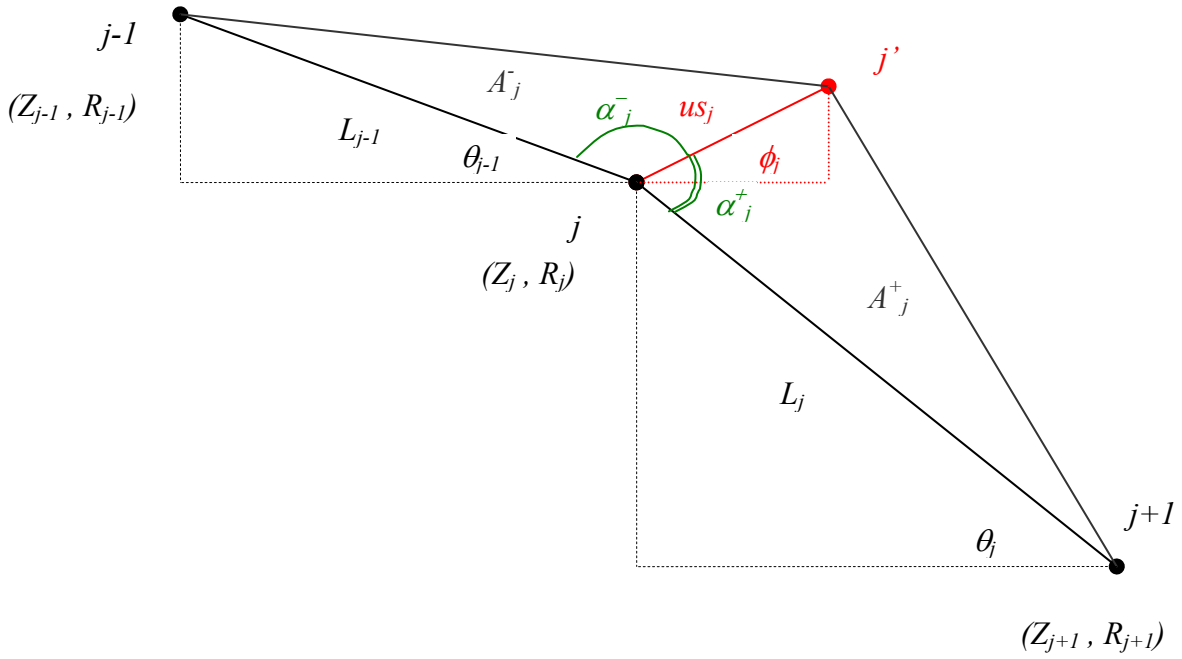

Figure 3: The infinitesimal volume change.

The two small areas can be then calculated as:

$$A_j^- = \frac{us_j L_{j-1}}{2} \sin \alpha_j^-$$

$$A_j^+ = \frac{us_j L_j}{2} \sin \alpha_j^+$$

and thus the total area in the R,Z plane is given by:

$$dA_j = \frac{us_j}{2}\left[L_j \sin\left(\phi_j + \theta_j\right) + L_{j-1} \sin\left(\phi_j + \theta_{j-1}\right)\right]$$

Finally, the infinitesimal volume change is given by:

$$dV_j = 2\pi R_j \, dA_j$$

For the points at the extremes of the geometry only the left or right triangles need to be considered for the area change.

2.3.2 K_L evaluation procedure

A small, home written, postprocessor reads the TBL file out of the Superfish postprocessor, containing the geometry and pressures and generates the input file for the structural simulation with ANSYS, which is run to produce the output file containing the geometrical displacements. As a final step a Mathematica notebook then has been written in order to read and parse the same TBL file for the geometry and Slater coefficient input and the ANSYS output for displacements. The Mathematica notebook evaluates the Slater analysis and produces a number of useful plots, shown below (MKS units). A 10 MV/m accelerating field is used for the calculations.

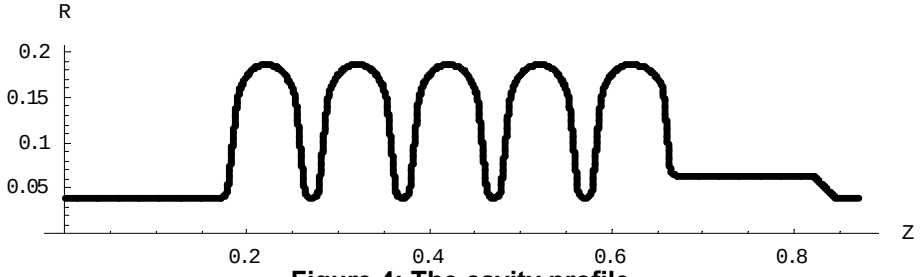

Figure 4: The cavity profile.

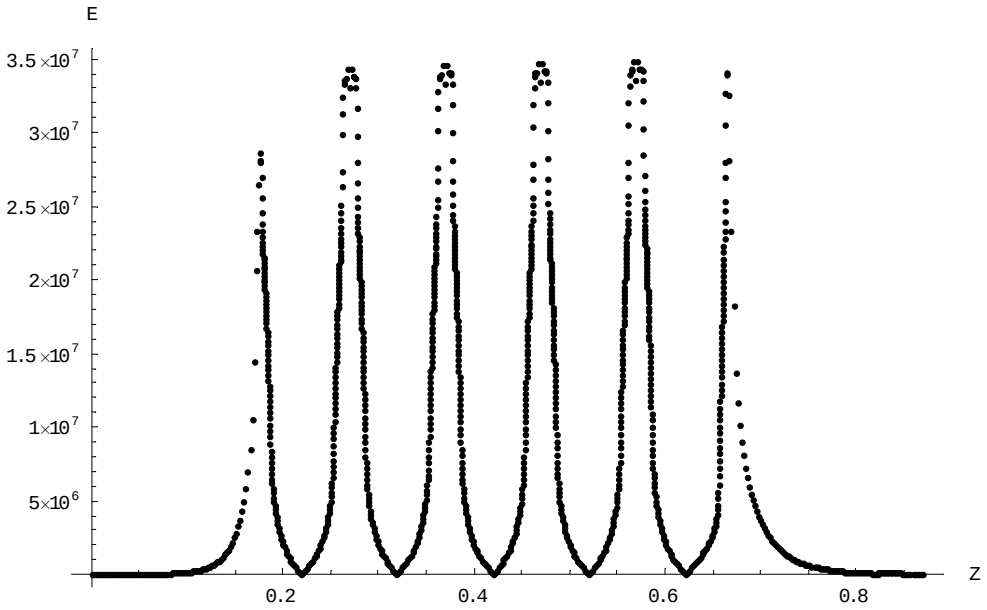

Figure 5: The surface electric field as a function of the longitudinal position.

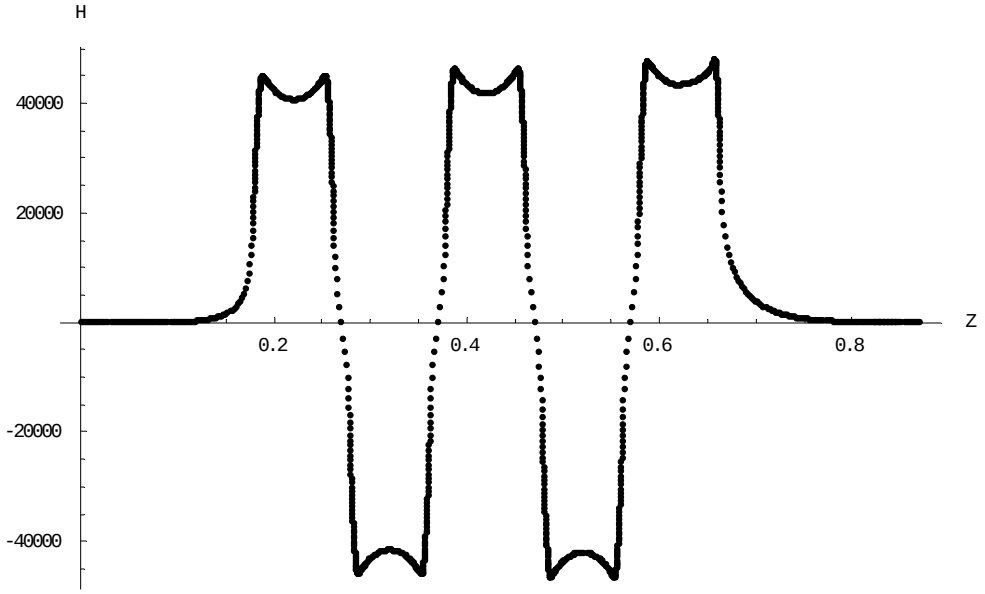

Figure 6: The surface magnetic field as a function of the longitudinal position.

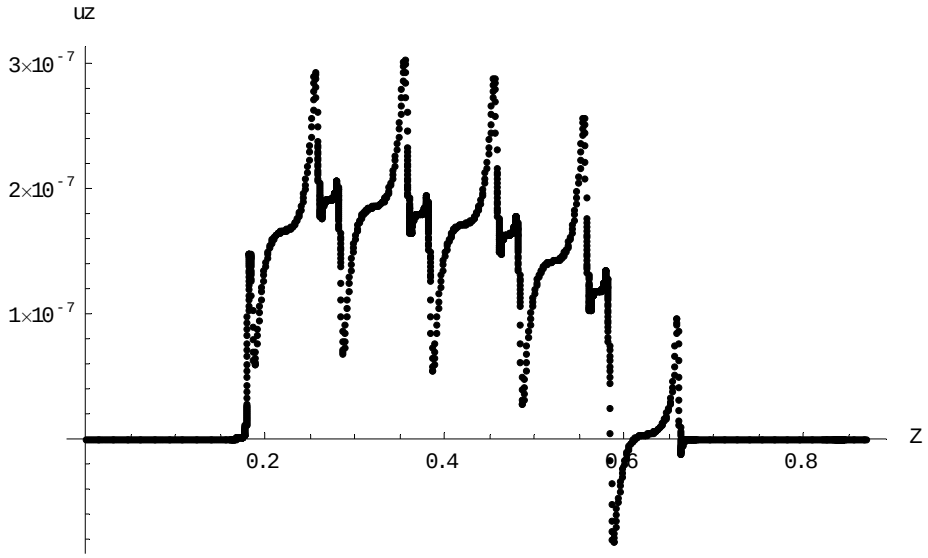

Figure 7: The longitudinal wall displacements

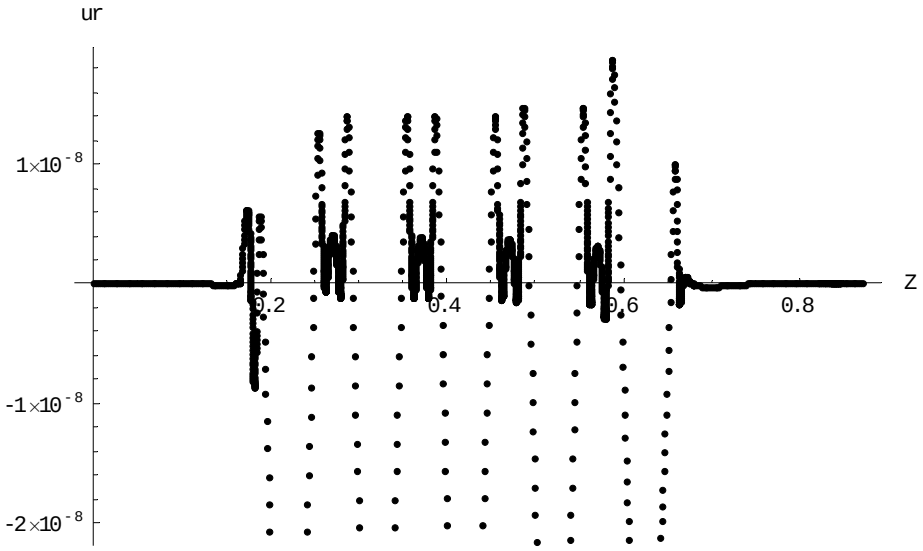

Figure 8: The radial wall displacements.

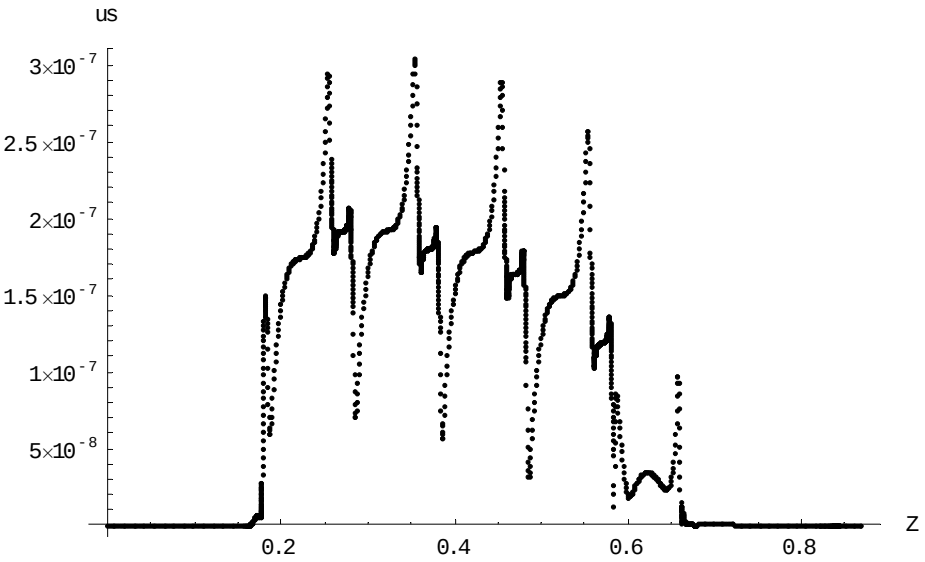

Figure 9: The length of the displacement vector.

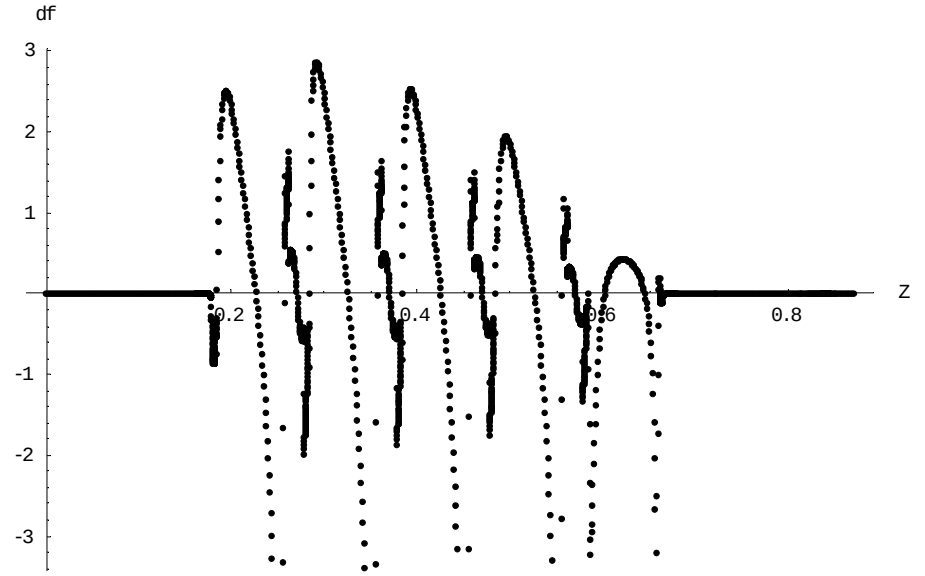

Figure 10: The infinitesimal frequency change, as a function of the longitudinal position.

The main part of the procedure, with the detuning and Slater coefficient evaluation is illustrated in the code below

```
L = Table[Sqrt[(Z[[j+1]]-Z[[j]])^2+(R[[j+1]]-R[[j]])^2],{j,1,nz-1}];
us = Sqrt[ uz^2 + ur^2];
Psi= Table[ArcTan[uz[[j]],ur[[j]]],{j,1,nz}];
Do[If[Psi[[j]]== Interval[{-p,p }],Psi[[j]]=0],{j,1,nz}]
Theta =Table[ArcTan[Z[[j+1]]-Z[[j]],R[[j]]-R[[j+1]]],{j,1,nz-1}];
dA=Table[0,{j,1,nz}];
dA[[1]]= 0.5 us[[1]] ( L[[1]] Sin[Psi[[1]]+Theta[[1]]]);
Do[ dA[[j]]=0.5 us[[j]]
    ( L[[j]] Sin[Psi[[j]]+Theta[[j]]] +
      L[[j-1]] Sin[Psi[[j]]+Theta[[j-1]]]), {j,2,nz-1}]
dA[[nz]]= 0.5 us[[nz]] ( L[[nz-1]] Sin[Psi[[nz-1]]+Theta[[nz-1]]]);
dV = 2π R dA;
df= Slater dV F0/W;
DeltaF=0;
Do[DeltaF = DeltaF+df[[j]],{j,1,nz}]
KL = DeltaF /100;
```

As an example, the accelerating field of 10 MV/m results in a $\Delta\nu$=370.702 Hz frequency shift, that is a LFD coefficient $\mathbf{K_L = -3.70701\ Hz/(MV/m)^2}$ for the "constrained" Lorentz force case. This procedure can also be easily implemented as an ANSYS script.

2.3.3 Other load cases

The procedure outlined above for the evaluation of the frequency shift is not limited to the changes induced by the mechanical pressure associated to the electromagnetic field, but can be used also for evaluating the sensitivity to deformations of the cavity boundary induced by any mechanical action. In this paper we have used the same procedure to evaluate the longitudinal frequency sensitivity and tuning coefficient, the vacuum coefficient, etc.

2.4 Mechanical characterization of the cavity

2.4.1 Parameters/methodology used in mechanical calculations

The table below lists all the model and material parameters used in the mechanical calculations.

Table 1: Parameters for mechanical calculations.

Parameter	Value	Units
Cavity wall thickness	4.0	mm
Niobium material		
Young Modulus, E_x	105	GPa
Density, ρ	8570	kg/m^3
Major Poisson ratio, ν_{xy}	0.4	-

Except where explicitly noted, all models are built using axisymmetric shell elements (SHELL51, with two nodes). A linear elastic model is used.

All parameters and dimensions are in MKS units.

All frequency changes resulting from a mechanical deformation of the cavity are evaluated by means of the Slater procedure discussed in the previous paragraph. Stress output, available from all cases, is not commented here.

2.4.2 Basic problem geometry in ANSYS

The problem geometry used in ANSYS is shown in the picture below. The (possibly) constrained points at the He tank support positions are indicated (as triangles) in the plot. This geometry is the same used for all load cases.

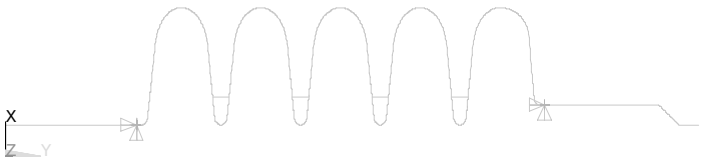

Two different models are obtained using this geometry, a simple uniform model where a 4 mm Nb thickness is used along all the cavity walls and a model where the cavity equator is reduced to 1.8 mm at the equator to allow the electron beam welding.

2.4.3 Uniform thickness model

The case of a uniform Nb thickness of 4 mm along all cavity profile is discussed first.

2.4.3.1 Spring and tuning coefficient of the structure

The spring coefficient of the cavity for a longitudinal compression has been evaluated with the ANSYS model obtained by the postprocessing of the Superfish output and showed before. By applying 0.1 mm compression at the smaller tube end, the longitudinal reaction force amounts to 124.84 N, and a 100 N load at the same position results in a displacement of 0.0801 mm. The cavity spring coefficient thus obtained is 1.248 kN/mm.
The following figure show the cavity displacement in the first case (cavity shortened by 0.1 mm), amplified by a factor 200.

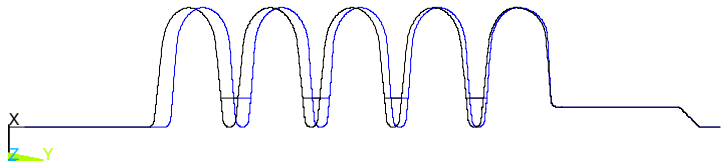

The associated frequency variation due to this deformation is $\Delta\nu$=-35,339.9 Hz, that is a frequency sensitivity coefficient of -353.4 kHz/mm (assuming δz is positive for a cavity compression). The frequency change has been evaluated by performing the Slater integral with the displacement produced by the ANSYS mechanical calculation. The results of this analysis are summarized in the following table.

Table 2:Cavity spring constant and frequency sensitivity (uniform thickness).

K_{cav}	1.248 kN/mm
$\partial f/\partial z$	-353.4 kHz/mm

2.4.3.2 Vacuum load calculations and frequency coefficient

By using a uniform pressure load (10^5 Pa, approx 1 atm) over the cavity and fixed cavity length boundary conditions, the following displacements are obtained (scale factor 200, maximum displacement is 159 μm.).

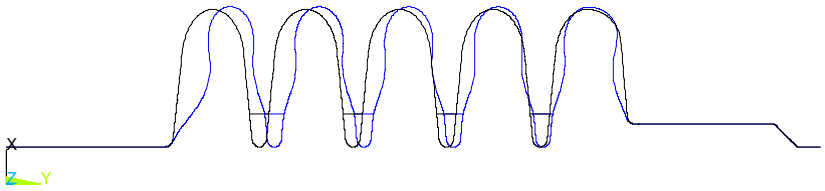

The computed frequency variation in this case is 84.72 kHz, that is giving a pressure coefficient of 84.72 Hz/mbar in the constrained geometry (frequency gets higher). The reaction force in the longitudinal direction acting on the cavity constaints is approximately 3.711 kN for a pressure load of 10^5 Pa. Linearity with a 100 Pa (~1 mbar) pressure load has been verified.
In the unconstrained case we have a relevant cavity shortening (2.98 mm, consistent with the reaction force found in the constrained case and the cavity spring constant), with a frequency shift of -966.05 kHz, i.e. -966.05 Hz/mbar. This case is shown in the following figure.

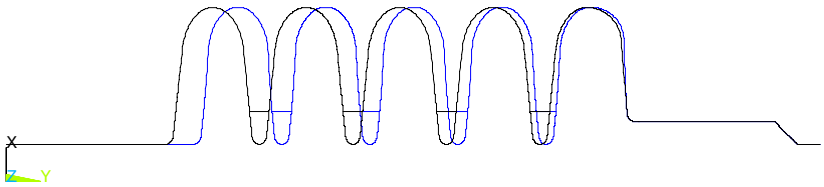

The results of the vacuum characterization is shown in the table below.

Table 3: Vacuum coefficient (uniform thickness).

Vacuum coefficient (fully constrained), $\Delta\nu_V^{\infty}$	+84.72 Hz/mbar
Vacuum longitudinal reaction, F_V^{∞}	3.711 N/mbar

This is in agreement with the linear superposition of the two effects: the shape deformation induced by the pressure on the constrained cavity and a cavity shortening due to a finite stiffness of the external constraints that try to maintain the cavity at the correct length. Assuming an external stiffening structure characterized by K_{ext}, the frequency displacement (in Hz/mbar) can be written as:

$$\Delta\nu_V = \Delta\nu_V^{\infty} + \frac{\partial f}{\partial z}\frac{F_V^{\infty}}{K_{ext}+K_{cav}}$$

2.4.4 Equatorial weld reduction

In the equatorial region the Nb thickness has been reduced to 1.8 mm, for 4 mm at each side from the nominal equatorial plane position.

2.4.4.1 Spring and tuning coefficient of the structure

The model used in this case is shown below (where shell elements are shown with their relative thickness. The same nodal coordinates of the previous model are used, but different parametric thicknesses are used in the regions.

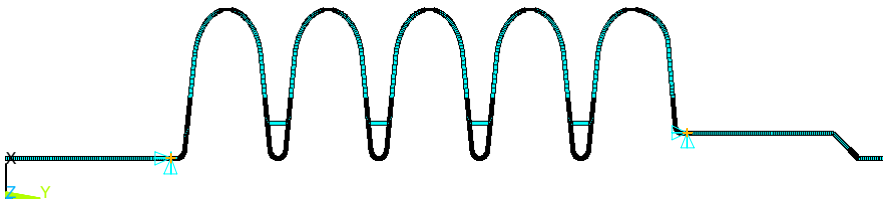

The analysis of this configuration leads to the following characterization:

Table 4: Cavity spring constant and frequency sensitivity (equatorial weld)

K_{cav}	1.226 kN/mm
∂f/∂z	-350.4 kHz/mm

2.4.4.2 Vacuum load calculations and frequency coefficient

The vacuum coefficient analysis is summarized by the following table:

Table 5: Vacuum coefficient (equatorial weld).

Vacuum coefficient (constrained)	+103.53 Hz/mbar
Vacuum longitudinal reaction	3.76 N/mbar

3 Mechanical characterization of the end dishes

Here we characterize the stiffness of the end dishes, under different loading configurations, corresponding to the "nominal" response when the He tank has been welded in place and to the JLAB RF tests case where the cavity is constrained longitudinally at the two dishes.
The two He tank dishes are shown below. On the left we show the end dish at the Fundamental Power Coupler (FPC) side (130 mm), with an outer diameter of 412 mm, and on the right the end dish at the smaller tube side (80 mm), with an outer diameter of 380 mm.

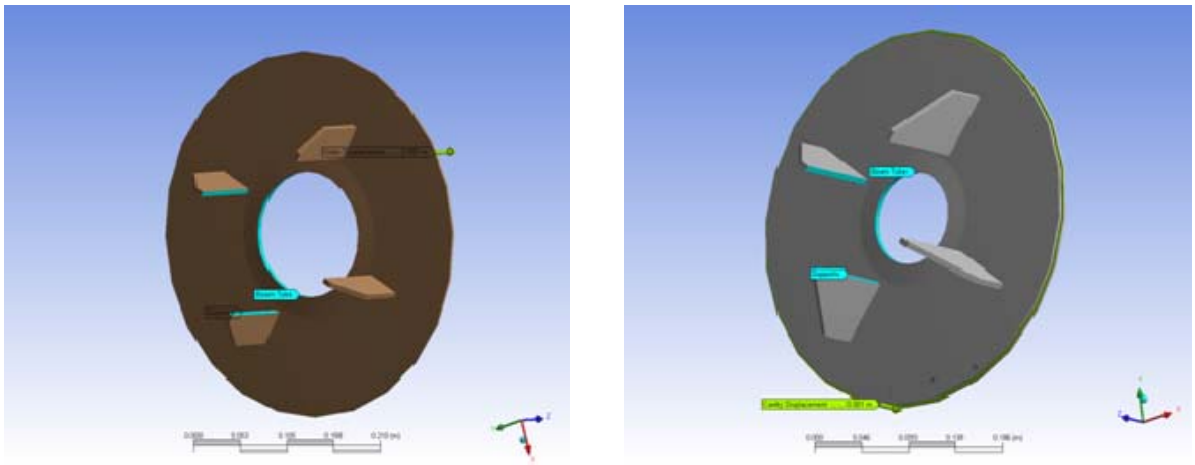

Figure 11: The two end dishes where the He tank is welded.

3.1 End Dish, FPC side

By imposing a displacement at the region where the He tank is welded to the dish, the structure reacts with a force of ~ 26 kN/mm. The displacement obtained is shown in the figure below, for a displacement of 1 mm (shortening the cavity).

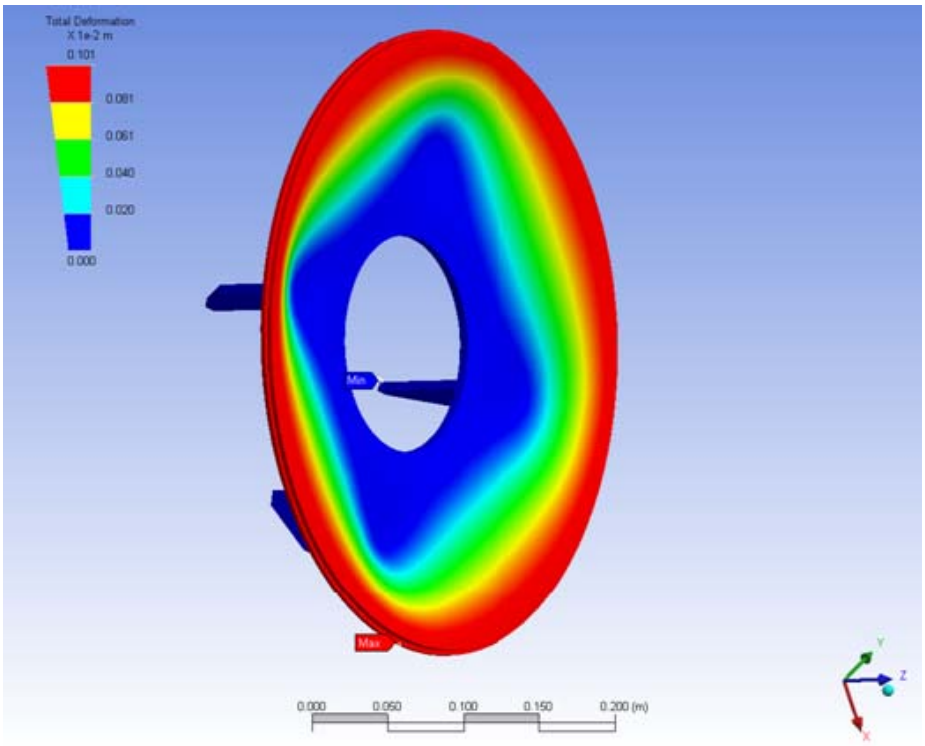

Figure 12: Deformations in the nominal load case, corresponding to the welded He tank.

However, in a loading condition similar to the situation described in the following paragraph, corresponding to the JLAB tests, the cavity is constrained by blocking the He tank dishes with two plates. By imposing such a loading condition, a much weaker stiffness is obtained, with a spring coefficient of approximately 2 kN/mm. This situation is illustrated in the following figure, where the system is loaded with 6 kN (1 kN for each contact pin) and the maximum displacement is nearly 3 mm in the position where the loads are applied.

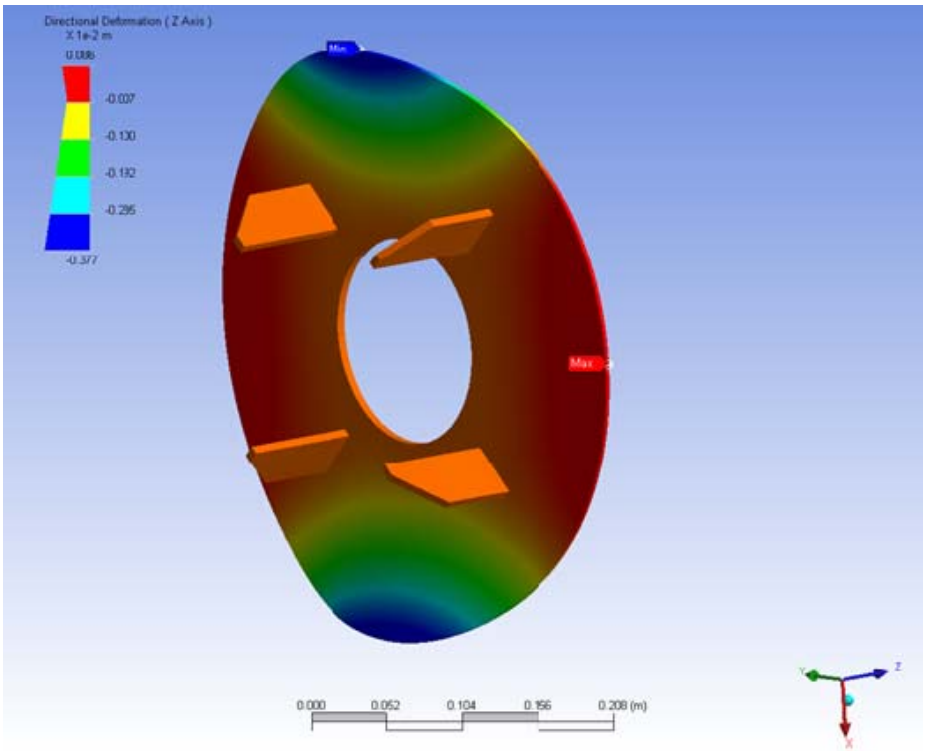

Figure 13: Deformations in the load case (130 mm tube side) during the JLAB RF tests.

3.2 End Dish, smaller tube side

Similar results are obtained for the analysis of the other end dish, which has a "natural" stiffness (i.e. when connected to the He tank) of ~ 40 kN/mm, but is much weaker under the JLAB frame load condition. Again, a load of 6 kN (1 kN at each support pin) produces a displacement of 2.8 mm in the contact region. The situation of this last load case is shown in the following figures, which illustrate the load condition and the longitudinal displacement produced.

3.3 Summary of end dish characterization

The following table summarizes the characterization of the end dishes under the different operating (load) conditions described in the preceding paragraphs.

Table 6: End dish spring coefficient characterization under different load conditions.

Large tube (FPC) side	
Nominal K_{Dbig}	26 kN/mm
JLAB load case	~ 2 kN/mm
Large tube (FPC) side	
Nominal K_{Dsmall}	40 kN/mm
JLAB load case	~ 2.1 kN/mm

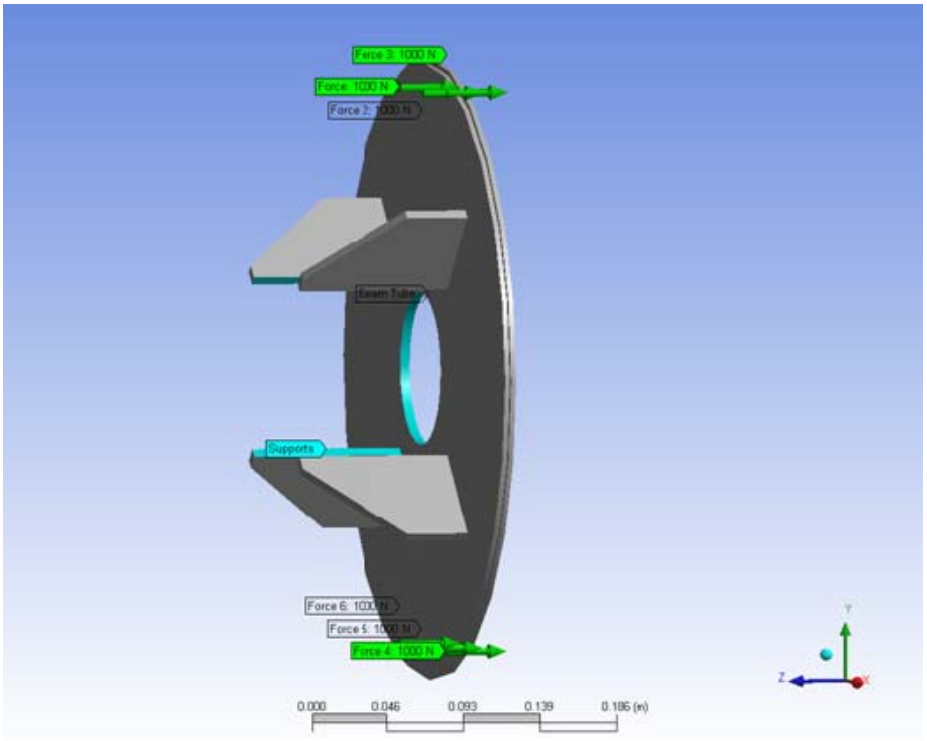

Figure 14: Load condition (80 mm tube side) during JLAB RF tests.

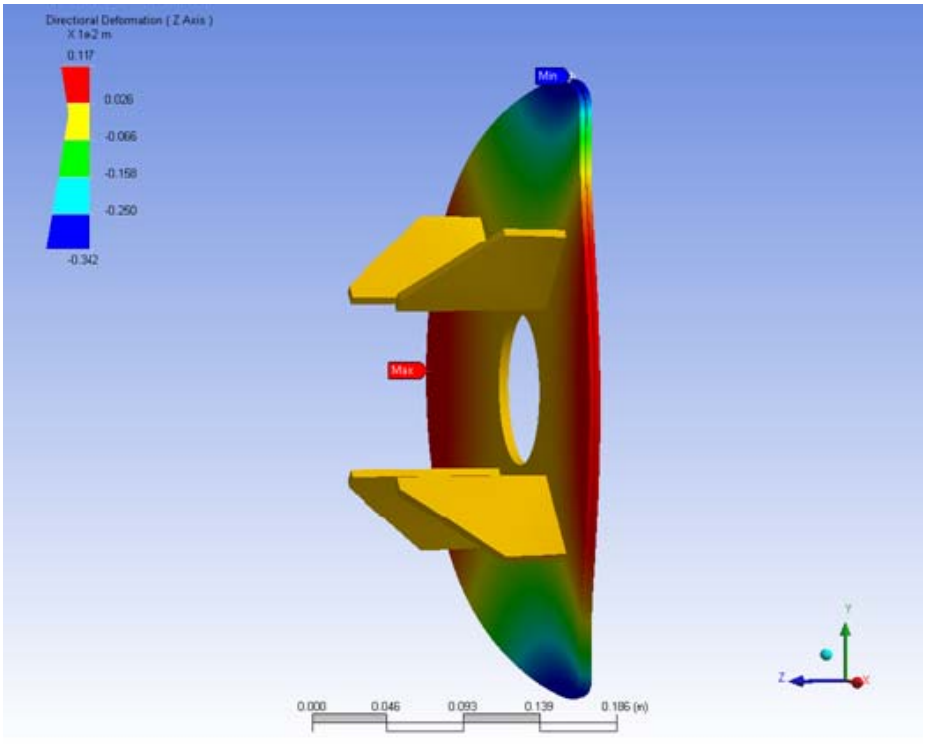

Figure 15: Deformations in the load case (80 mm tube side) during the JLAB RF tests.

4 Mechanical characterization of the He tank

The helium tank is a titanium reservoir connected to the cavity end dishes and, in order to allow the longitudinal tuner action on the cavity is made two cylindrical parts connected by a bellow in the central region.
The tank is slid on the cavity at the smaller end dish side, where an adaptation ring allows the welding. One of the two cylindrical parts is split in two parts, in order to adjust the final length to the cavity before the final weldings.
The cylindrical parts are used to support the tuner mechanism. This section is dedicated to the mechanical characterization of the He tank.

4.1 Parameter used in mechanical computations

The table below lists all the material type and parameters used for the mechanical calculations.

Table 7: Parameters for mechanical calculations.

Parameter	Value	Units
Helium tank and connection rings material	Ti Gr2	-
Bellow material	Ti Gr1	-
Titanium Grade 1 material		
Young Modulus, E_x	105	GPa
Density, ρ	4500	kg/m^3
Major Poisson ratio, ν_{xy}	0.37	-
Titanium Grade 2 material		
Young Modulus, E_x	105	GPa
Density, ρ	4500	kg/m^3
Major Poisson ratio, ν_{xy}	0.37	-

The finite element model used for the characterization, is made of axisymmetric shell elements (SHELL51, with two nodes). A linear elastic model is used.

4.2 Geometry

The overall geometry of the He tank is reported in Figure 16.
The finite element models were built with some simplification as described in the following sections.

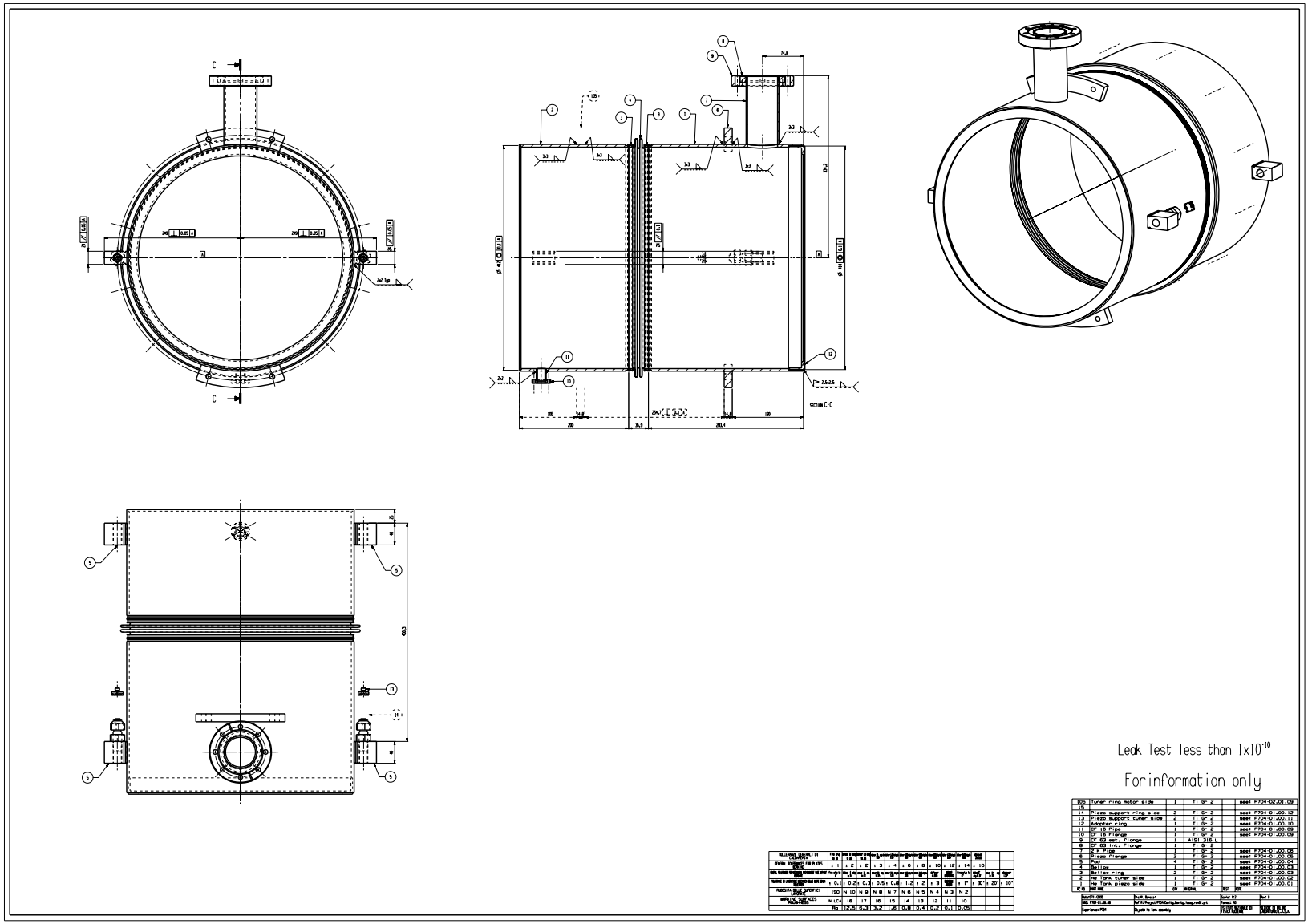

Figure 16: The He tank geometry.

4.3 Helium tank analysis without bellow

In order to evaluate the axial stiffness of the tank and of its adaptation ring a finite element analysis has been performed. The bellow has not been considered in this model and its characteristics will be evaluated in paragraph 4.4.
The finite element model is reported in Figure 17. It consists of 28 axisymmetric shell element and 29 nodes. By imposing an axial displacement of 1 mm at the right side, the helium tank reacts with a force of 856 kN, yielding a stiffness of 856 kN/mm. The displaced geometry (with a magnification factor of 200) is shown in Figure 18.

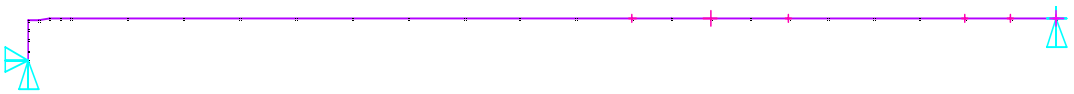

Figure 17: Helium tank mesh (without bellow).

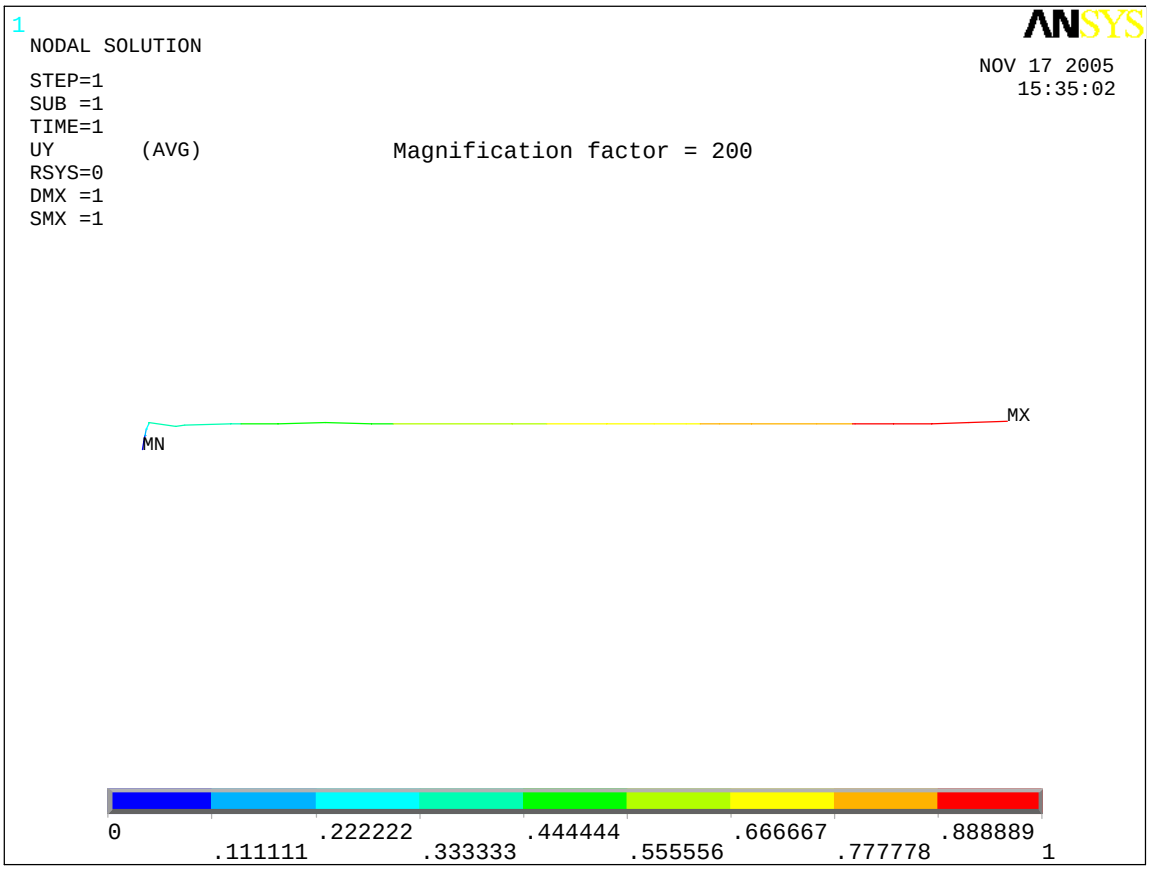

Figure 18: Helium tank stiffness analysis: deformed mesh.

4.4 Helium tank bellow

The finite element model of the bellow is shown in Figure 19. It is made of 88 axisymmetric shell elements and 89 nodes.

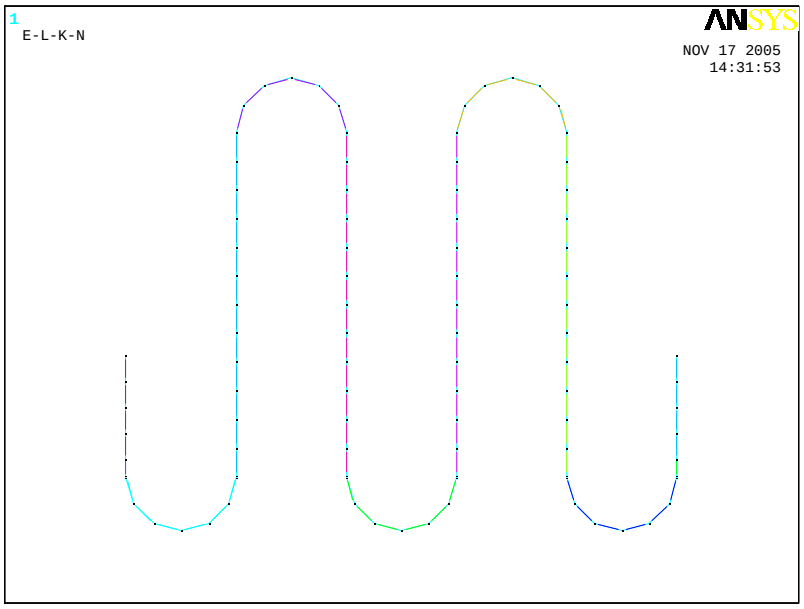

Figure 19: Helium tank bellow: finite element mesh

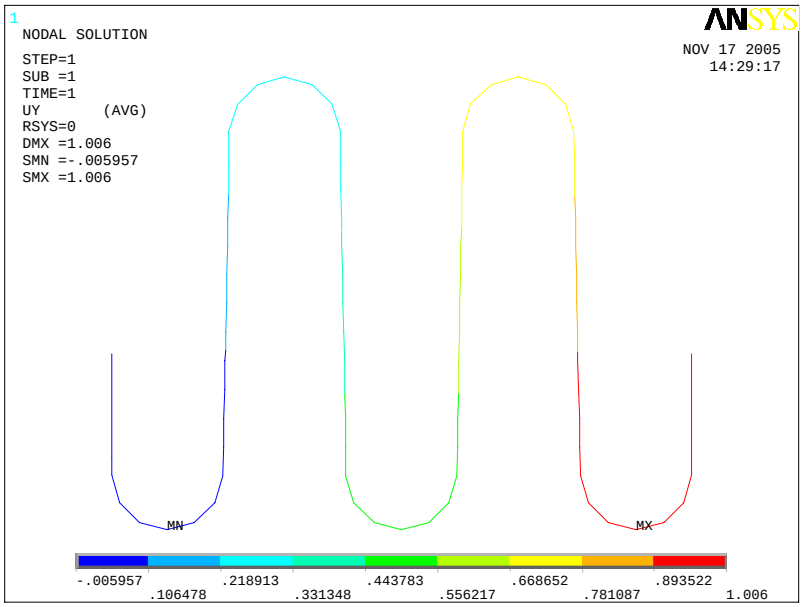

Figure 20: Helium tank bellow: deformed mesh

By imposing an axial displacement of 1 mm at the right side, the bellow reacts with a force of 0.312 kN, yielding a stiffness of 312 N/mm. The displaced geometry is shown in Figure 20.

5 Mechanical characterization of the Piezo Blade Tuner

The coaxial piezo blade tuner has been scaled from the concept proposed for the TESLA and ILC projects [6] and successfully tested for the slow tuning of the TTF superstructures [7]. A similar effort for the design and construction of a fast-slow tuner for 1.3 GHz superconducting structures is being carried out in the context of the CARE-SRF Joint Research Activity and has been reported in [8].The tuner consists of three main components:

- the rings-blades assembly, that provide the cavity slow tuning action;
- the leverage mechanism, that, equipped with a stepping motor, drives the rings-blade assembly;
- the piezo actuator part, that, during operation, provides the fast tuning action necessary for Lorentz Force Detuning compensation under pulsed operation.

These three parts will be analyzed and explained in depth in the following sections.

5.1 Parameters used in mechanical calculation

The material characteristics used for the mechanical analyses are reported in Table 8.

Table 8: Mechanical characteristics used for the tuner analysis.

Parameter	Value	Units
Rings material	Ti Gr2	-
Blade material	Ti Gr5	-
Jaw with pin, operating bracket	AISI 316L	-
Motor and bearing support	AISI 316L	
Connecting rod	Brass, Ot MS58	-
Titanium Grade 2/5 material		
Young Modulus, E_x	105	GPa
Density, ρ	4500	kg/m^3
Major Poisson ratio, ν_{xy}	0.37	-
Aisi 316L		
Young Modulus, E_x	191	GPa
Density, ρ	7850	kg/m^3
Major Poisson ratio, ν_{xy}	0.29	-
Ot MS58		
Young Modulus, E_x	105	GPa
Density, ρ	8400	kg/m^3
Major Poisson ratio, ν_{xy}	0.35	-

5.2 Geometry of all parts

The geometry of the main tuner parts is shown in the following technical drawings:

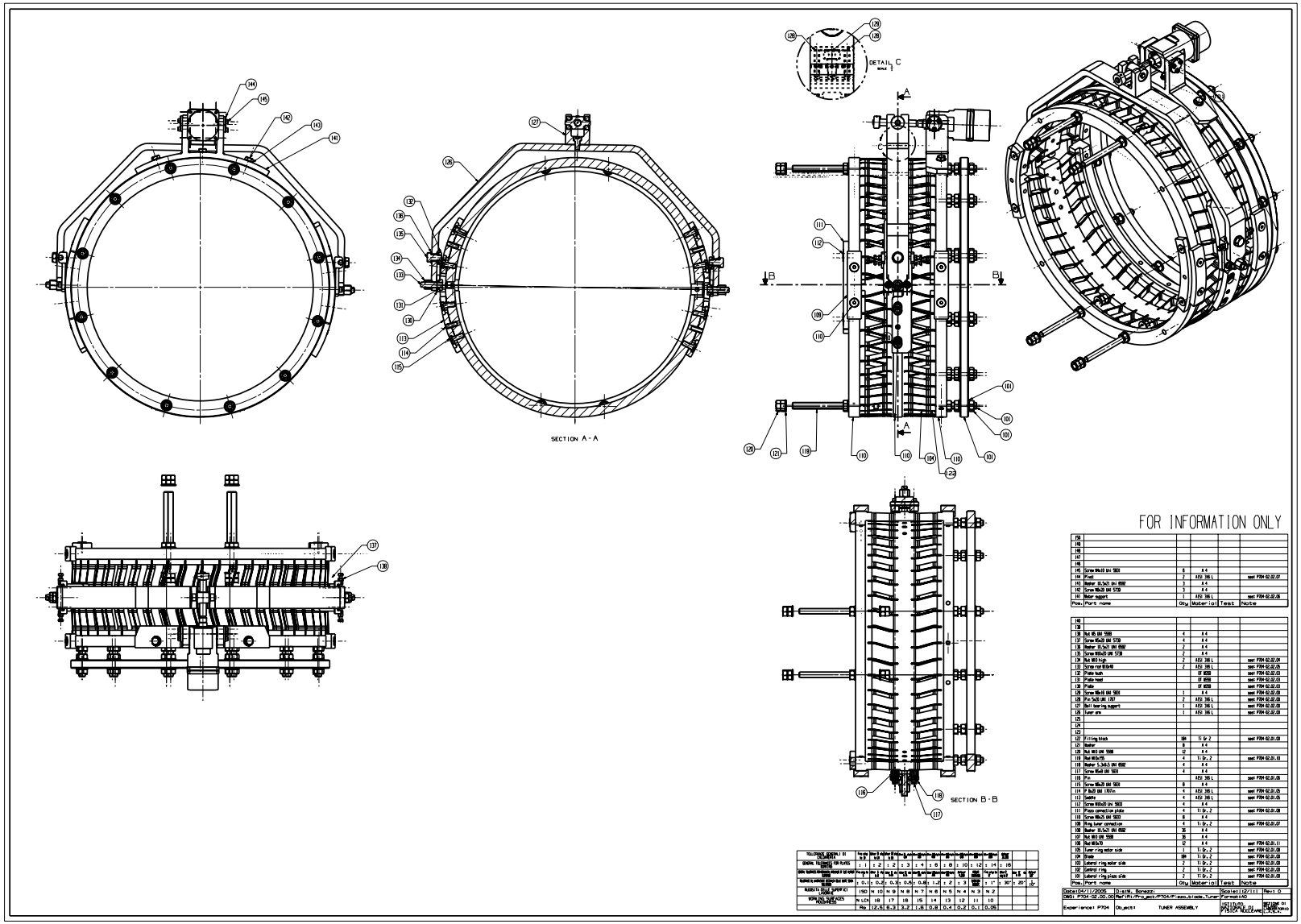

Figure 21: The piezo blade tuner assembly.

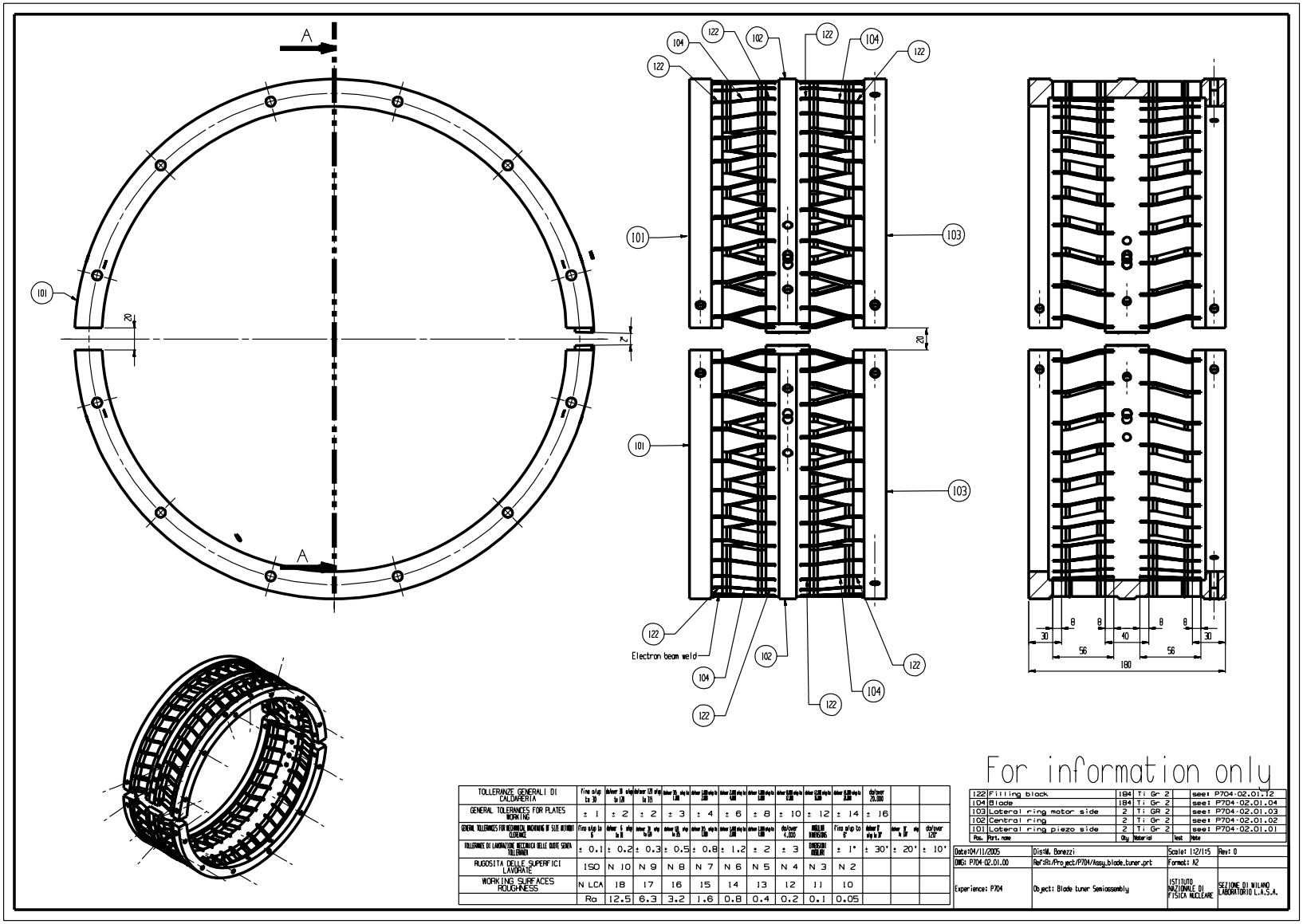

Figure 22: The rings-blade tuner assembly.

5.3 Mechanical characterization of leverage

5.3.1 Leverage kinematics

The working principle of the tuner is based on the deformation of the blades from the rest position (slant of 16° respect to the cavity axis) to a different configuration producing an axial elongation or shortening of the tuner itself (see Figure 23 for the symbols).

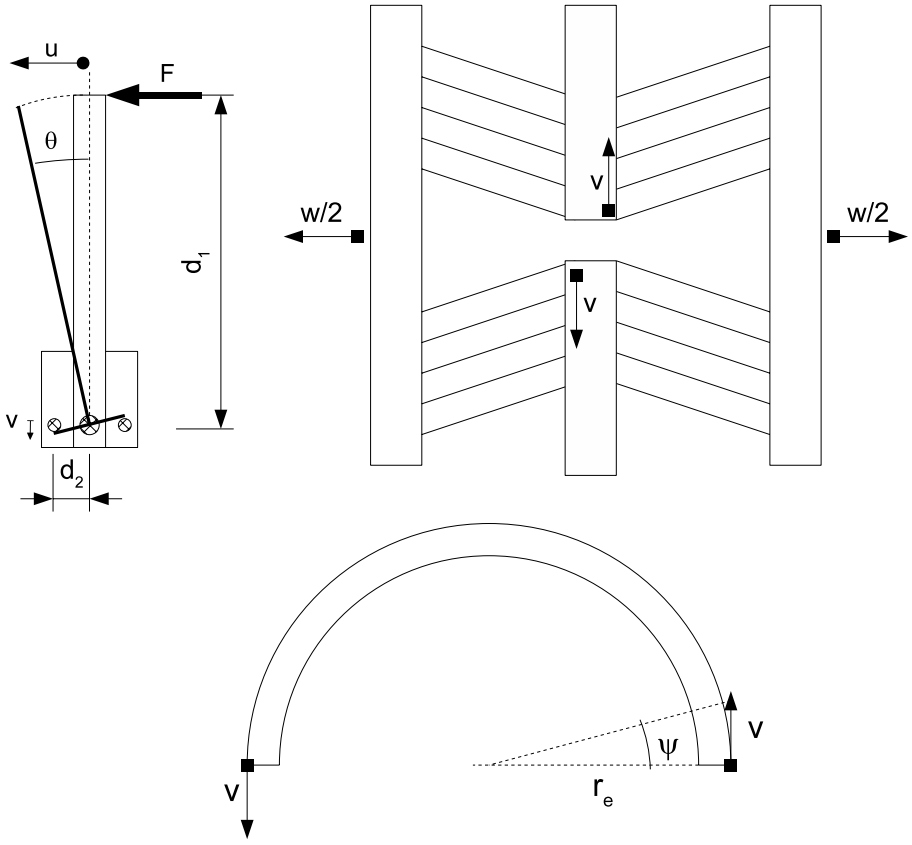

Figure 23: Kinematic description of the ring-blade assembly for the cold tuning system

This longitudinal movement, *w*, is generated by the rotation, by the angle ψ or the corresponding movement of the ring ends *v*, of the central rings with respect to the lateral ones, which are fixed to the He tank. In order to reduce to a negligible value the relative rotation of the lateral rings and to balance the torsional moments, the two (upper and lower) central rings rotate in opposite directions and the blade are assembled symmetrically with respect to the horizontal plane.

Finally, the rotation ψ of the central ring is driven through a stepping motor that exerts a force *F* on the leverage arm, which in turn transforms the displacement *u*, through a specially designed connecting plate, into the azymuthal movement *v* of the rings.

For the TRASCO Cavity A, we have used the following values for the ring dimensions used in Figure 23:

$$d_1 = 249.5 + 12 + 40 = 301.5\,\text{mm}$$
$$d_2 = 70/2 = 35\,\text{mm}$$
$$r_e = 476/2 = 238\,\text{mm}$$

and, from simple geometrical considerations we can write the following relationships:

$$\theta = \arctan\frac{u}{d_1}$$

$$v = d_2 \tan\theta = u\frac{d_2}{d_1}$$

$$\psi \cong \frac{v}{r_e} = \frac{u}{r_e}\frac{d_2}{d_1}$$

The maximum displacement that can be applied along the *v* coordinate is limited by three factors: the maximum allowed blade deformations, the contact of the central rings themselves and the maximum movement of the leverage mechanism:

- **Maximum blade deformation**
  The two straight sections at each blade end have a distance of 7.5 mm, thus the maximal *v* displacement is reached at 8 mm, when the blade is deformed to a nearly straight geometry.
- **Limit displacement by contact of the central rings**
  The distance between the central rings is 25 mm, therefore, neglecting the small deformations of the leverage mechanism:

$$v_{\max} = 14/2 = 7.0\,\text{mm} \Rightarrow \psi_{\max} = \frac{7.0}{238} = 0.0294^r = 1.68°$$

$$u_{\max} = 7\frac{301.5}{35} = 60.3\,\text{mm}$$

- **Limit displacement imposed by leverage mechanism capabilities**
  The limiting part of the leverage mechanism capabilities is the connecting plate which has two slot with eccentricity of 1.25 mm (see Figure 24).

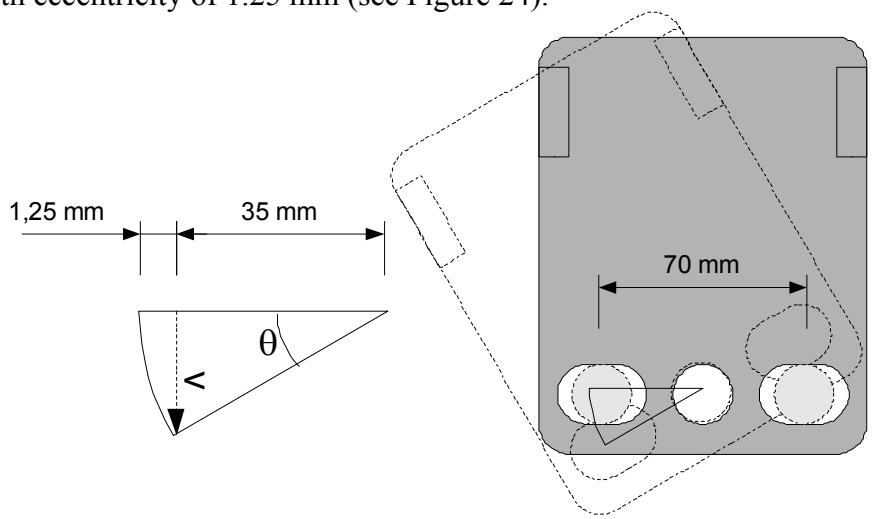

Figure 24: Details of the connecting plate kinematics.

With simple geometric considerations and neglecting again the small leverage mechanism deformations one obtains:

$$\theta_{\max} = \arccos\frac{35}{36.25} = 15° \Rightarrow v_{\max} = 36.25\sin\theta_{\max} = 9.4\,\text{mm}$$

$$\text{u}_{\max} = d_1 \sin\theta_{\max} = \pm 78\,\text{mm}$$

The limiting value of *v* set by the contact of the central rings is lower than the maximum tolerable blade deformation, thus allowing a safe operation of the tuner in all cases.

Finally, in order to evaluate the maximum axial displacement of the tuner, *w*, a finite element analysis is mandatory to take in account the possible effect of the leverage deformations.

5.3.2 Finite element model

Due to the complexity of the mechanism a simplified model has been used: some parts were neglected and, when possible, the connections have been considered as bonded. The boundary conditions imposed in the ANSYS simulation are shown in Figure 25, while the finite element model is reported in Figure 26.

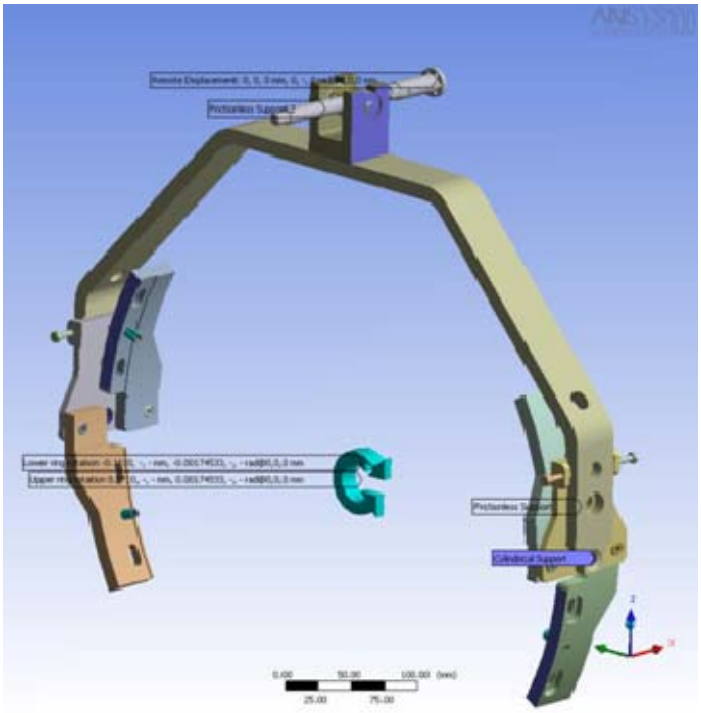

Figure 25: Boundary conditions applied to the leverage mechanism.

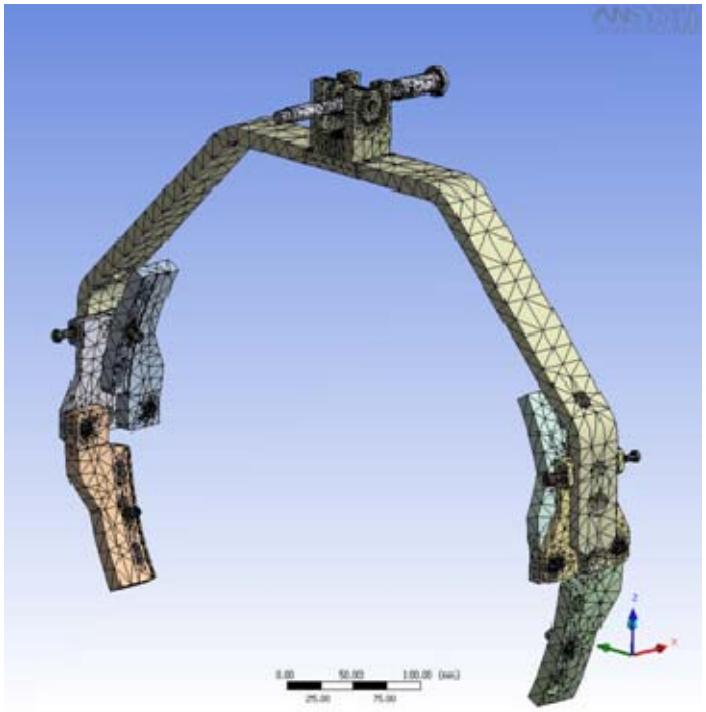

Figure 26: Finite element model of the leverage mechanism.

5.3.3 Leverage analysis

A finite element analysis of the leverage system has been performed in order to evaluate its stiffness and the maximum stresses. These results are then used with the results of the blade tuner rings discussed in paragraph 5.4 in order to obtain the behavior of the whole tuning system.
The analysis has been performed by imposing a rotation of 0.1° to the saddles connected to the central rings of the tuner while the driving shaft is constrained at its far end.
The reaction at the saddle has the same meaning of 2 Mz indicated in Figure 34. The results obtained is

$$2\,\mathrm{Mz} = 1228\ \mathrm{Nm}$$

And gives a total stiffness of:

$$k_{mech} = \frac{1228}{0.00174} = 703592\ \mathrm{Nm}$$

where we have considered the rotation of the central rings in the stiffness calculation.
The displacements and Von Mises stresses obtained from the model are reported in Figure 27 and Figure 28.

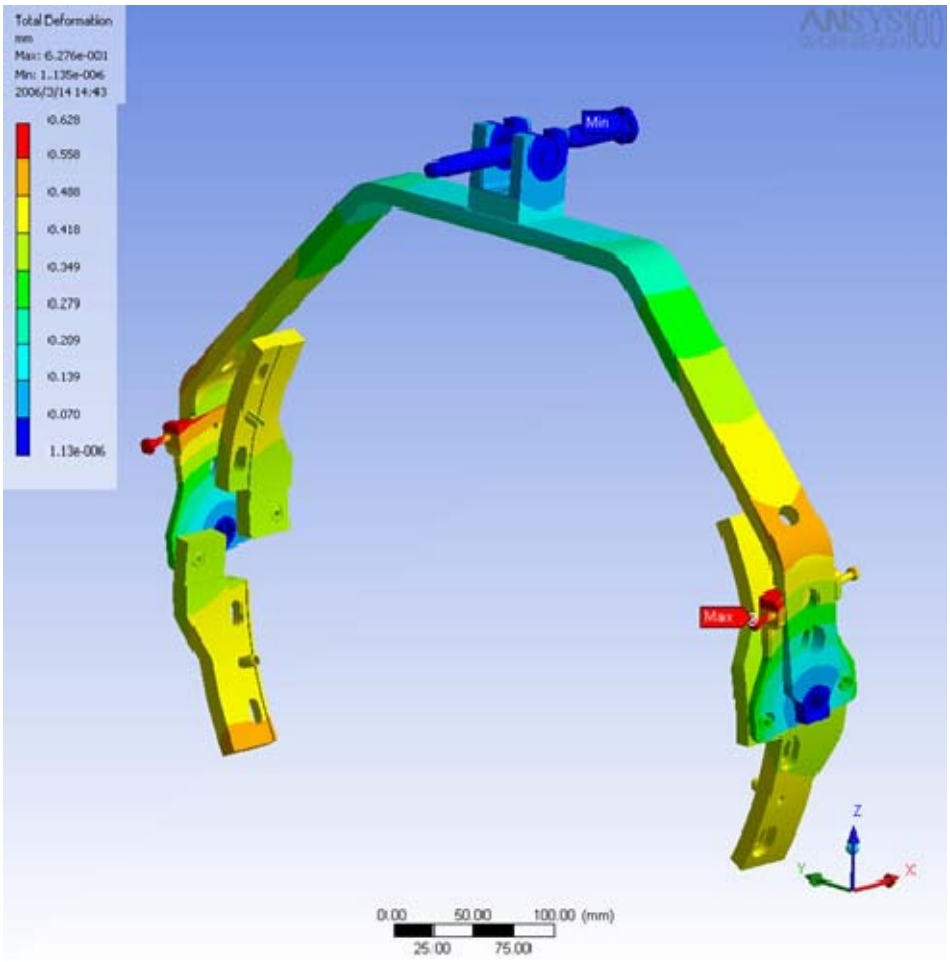

Figure 27: Displacements of mechanism.

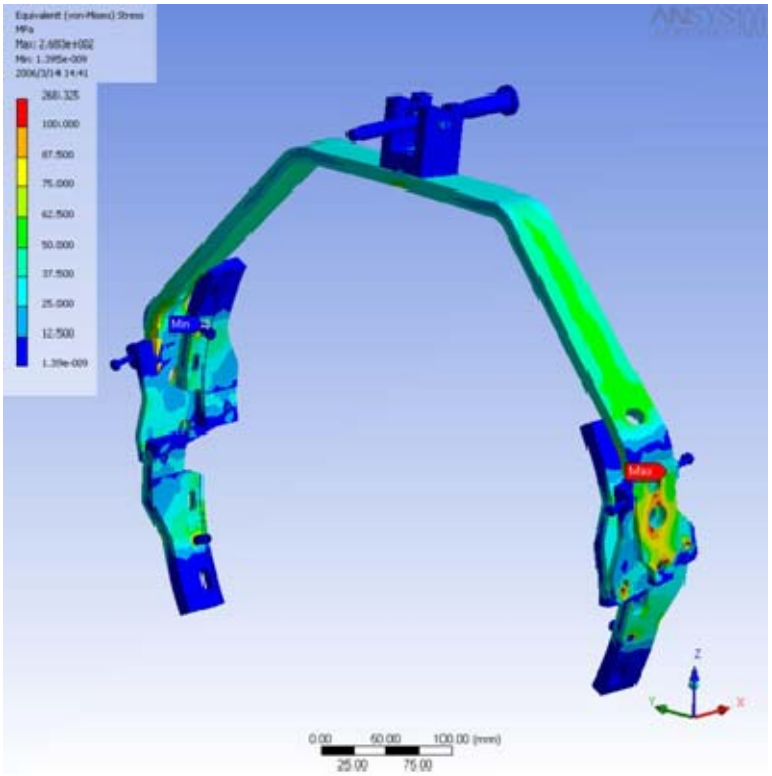

Figure 28: Von Mises stresses of mechanism.

5.4 Mechanical characterization of blade tuner

The blade tuner, used for the frequency tuning of the cavity, is composed of two parts which are symmetric with respect to the horizontal plane. The two parts, that in the following will be called half-tuner, are made of three rings and two series of blades, positioned symmetrically with respect to the central ring (see Figure 22). This configuration allows obtaining an axial movement of the lateral rings by means of an opposite rotation of the two central ones. Torsion and shear forces on the helium tank are thus minimized.

5.4.1 Tuner axial range

The blades transform the azimuthal rotation of the central ring into an axial elongation of the whole tuner. Figure 29 reports the tuner displacement as a function of the shaft displacement driven by the stepping motor. The "theoretical" curve has been obtained by a FEM analysis of the single blade behavior (described later in paragraph 5.4.3) coupled with the leverage kinematics already discussed in paragraph 5.3.1. Experience with measurements performed on the blade tuner already built with for the 1.3 GHz cavities shows that non idealities and a finite stiffness of the leverage mechanism reduce the range by approximately 20% with respect to the FEM estimations. This effect has been taken into account in Figure 29 into the "expected" data curve, which has been lowered by a 20% from the values obtained from the model.

Thus, with the actual leverage configuration, the tuner is capable of a maximum elongation of approximately 1.3 mm.

We note that if either a larger tuning range or a smaller shaft excursion is needed, this can be obtained by a suitable modification of the blade length/inclination and of the leverage mechanism, increasing the distance d_2 shown in Figure 23 and the connecting part shown in Figure 24.

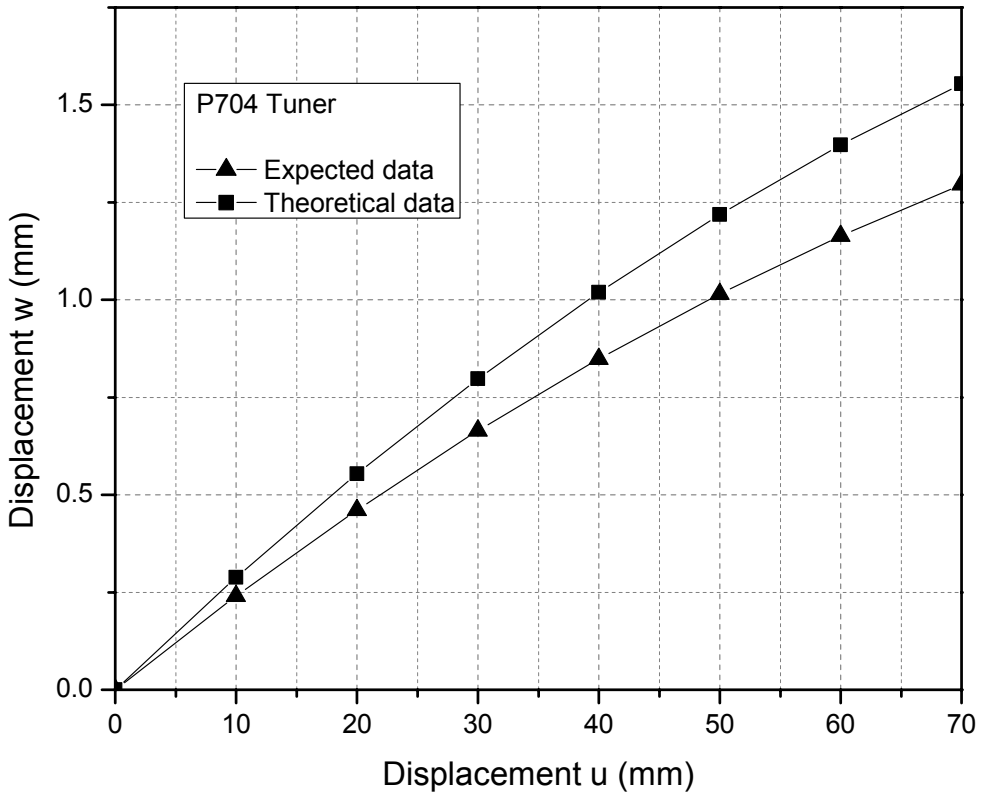

Figure 29: Maximum tuner displacement as a function of the shaft displacement.

5.4.2 Finite element model

Two different finite element models were considered: the first is a 2D model for the blade alone (see Figure 30) and the second is a 3D model for the half tuner (see Figure 31).
The blade model consists of 44 nodes and 43 beam elements, while the half tuner model consists of 81059 nodes, 48659 body elements and 4467 contact elements.
The next two paragraphs outline the characterization performed with these models, in order to derive the overall tuner stiffness.

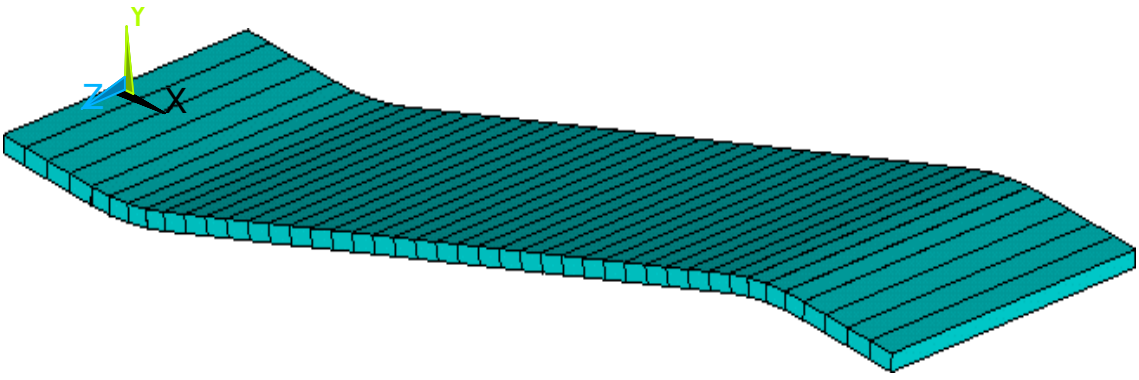

Figure 30: Finite element model of the single blade.

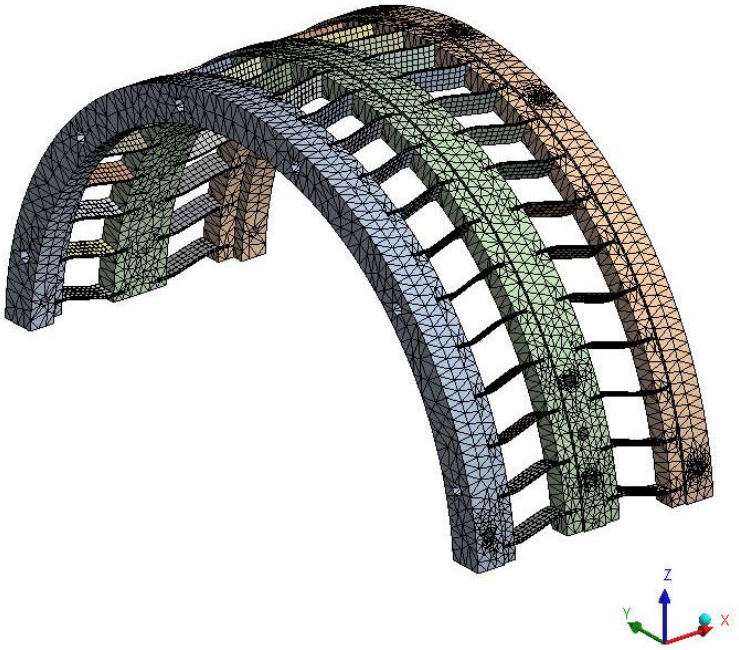

Figure 31: Finite element model of half tuner.

5.4.3 Single blade analysis

The 2D model of the blade allows considering only the in-plane deformations. Nevertheless a useful estimation of the tuner stiffness can be obtained by performing three analyses with different boundary conditions. The three cases, showed in Figure 32, represent the possible tuner behavior when all symmetries have already been considered. The following values are obtained:

Table 9: Single blade analysis results.

Load case	Δu (mm)	Δv (mm)	F_y (N)	M (Nmm)
1	-0.12879	0.49196	1	-19.965
2	-0.03306	0.12711	0	-4.154
3	-0.00052	0	0.2539	0.9835

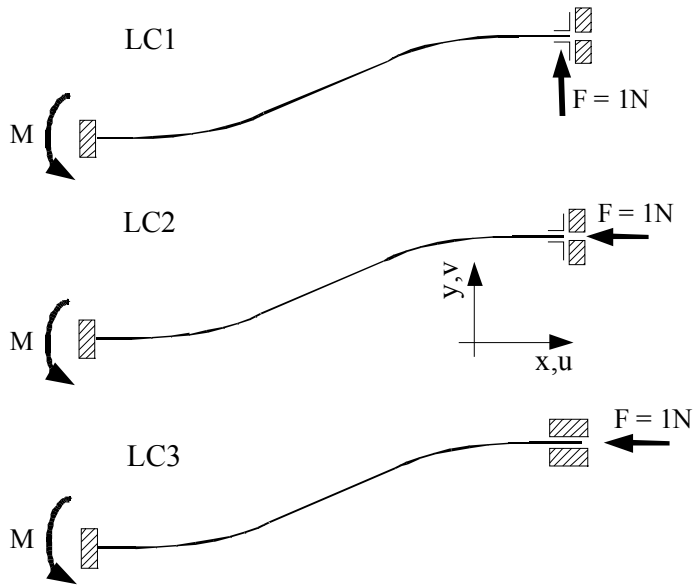

Case 1: central ring rotation

Case 2: axial compression with central rings free to rotate

Case 3: axial compression with central rings fixed

Figure 32: Load cases considered for the single blade analysis.

Considering that 2x2x23 = 92 blades are used for each half tuner the following compliance and stiffness are obtained:

- Load case 1: rotation of the central ring without constraints

$$C_{blade}^{mix} = \frac{\Delta u}{F \cdot r_b} = \frac{-0.01288}{1 \cdot 228.5} = -5.64E-5\,[\mathrm{N^{-1}}]$$

$$C_{blade}^{rot} = \frac{\arcsin\frac{\Delta v}{r_b}}{F \cdot r_b} = \frac{\arcsin\frac{0.49196}{228.5}}{1 \cdot 228.5} = 9.417E-6\,[\mathrm{N^{-1}mm^{-1}}]$$

$$C_{half-tuner}^{mix} = \frac{2}{92} C_{blade}^{mix} = -1.225E-6\,[\mathrm{N^{-1}}]$$

$$C_{half-tuner}^{rot} = \frac{1}{92} C_{blade}^{rot} = 1.023E-7\,[\mathrm{N^{-1}mm^{-1}}]$$

- Load case 2: compression of the tuner with the central ring free to rotate

$$C_{blade}^{mix} = \frac{\arcsin\frac{\Delta v}{r_b}}{F} = \frac{\arcsin\frac{0.12711}{228.5}}{1} = 5.56E-4\,[\mathrm{N^{-1}}]$$

$$C_{blade}^{ax-free} = \frac{\Delta u}{F} = \frac{-0.03306}{-1} = 3.306E-2\,[\mathrm{N^{-1}mm}]$$

$$C_{half-tuner}^{mix} = \frac{1}{46} C_{blade}^{mix} = 1.209E-5\,[\mathrm{N^{-1}}]$$

$$C_{half-tuner}^{ax-free} = \frac{2}{46} C_{blade}^{ax-free} = 1.437E-3\,[\mathrm{N^{-1}mm}]$$

- Load case 3: compression of the tuner with the central ring fixed

$$C_{blade}^{ax} = \frac{\Delta u}{F} = \frac{-0.00052}{-1} = 5.2E-4\,[\mathrm{N^{-1}mm}]$$

$$C_{half-tuner}^{ax} = \frac{2}{46} C_{blade}^{ax} = 2.261E-5\,[\mathrm{N^{-1}mm}]$$

where:

r_b = mean radius of blades on tuner,
C^{mix} = axial compliance due to a rotation of the central ring, or viceversa,
C^{rot} = torsional compliance due to a rotation of the central ring,
$C^{ax\text{-}free}$ = axial compliance due to an axial displacement of the free central ring,
C^{ax} = axial compliance due to an axial displacement of the central ring

5.4.4 Half tuner analysis

The 3D analysis allows considering all possible boundary conditions. Keeping in mind the symmetries of the tuner, generalized displacements have been considered that can describe the relative movement of the central ring with respect to the lateral ones. These displacements (two translations and one rotation) are reported in Figure 33. The symbol *u* and *w* refer to the displacement in *x* and *z* directions, while ψ refers to the rotation around the *z* axis.

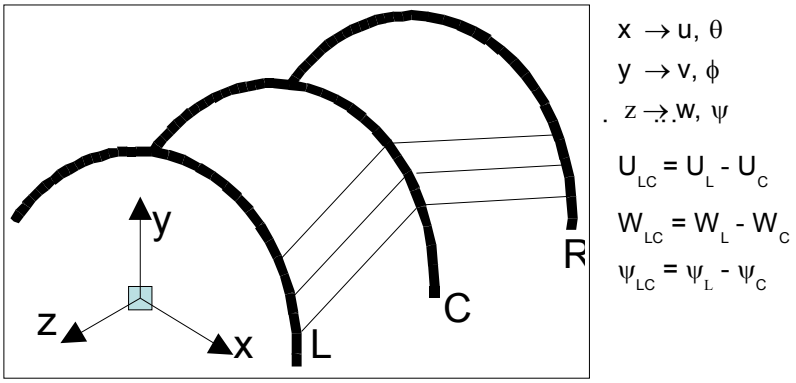

Figure 33: Generalized displacements for the half tuner.

Generalized forces are also introduced and associated to the respective relative displacement as explained in Figure 34.
By performing several analyses with only one generalized displacement active the following forces-displacements relations, relative to half tuner, have been obtained:

$$\begin{Bmatrix} \hat{Fx} \\ \hat{Fz} \\ \hat{Mz} \end{Bmatrix} = \begin{bmatrix} 10355 & 19427 & -1130096 \\ & 134950 & -7719500 \\ & & 449650000 \end{bmatrix} \begin{Bmatrix} u_{LC} \\ w_{LC} \\ \psi_{LC} \end{Bmatrix}$$

$$(\mathrm{N}, \mathrm{Nmm}) \qquad\qquad (\mathrm{mm}, \mathrm{rad})$$

In these relations *Fx*, *Fz* and *Mz* are opposite to the reactions obtained by the finite element analyses and the symbol ^ is used when only one half of the tuner is considered. This matrix is the stiffness matrix of the half tuner when all symmetries are considered.
The compliance matrix can then be easily obtained:

$$\begin{Bmatrix} u_{LC} \\ w_{LC} \\ \psi_{LC} \end{Bmatrix} = 10^{-6} \begin{bmatrix} 133.08 & -1.4356 & 0.3098 \\ & 412.695 & 7.0814 \\ & & 0.1246 \end{bmatrix} \begin{Bmatrix} \hat{Fx} \\ \hat{Fz} \\ \hat{Mz} \end{Bmatrix}$$

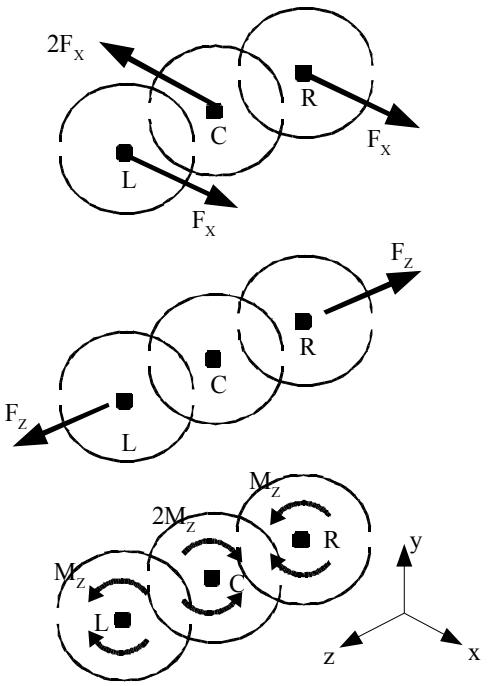

Figure 34: Diagram of the tuner forces.

5.4.5 Extensions of the analyses to the whole tuner

The stiffness matrix of the half tuner is here used to evaluate the behavior of the whole blade tuner (only ring-blade system, without mechanism and piezo actuator elements). The following assumptions are made:

- only the degree of freedom in the axial direction is considered between the two lateral rings;
- torsion, transversal force in the *x* direction and the associated displacements are relative to the central ring and are necessary in order to evaluate the behavior of the tuner equipped with the leverage mechanism;
- $w_{LR}=w_L-w_R$
- $w_{LC}=w_{CR}=w_{LR}/2$
- $u_{LC}=-u_{CR}$
- $\psi_{LC}=-\psi_{CR}$

It is easier to express the relation in terms of known forces applied to the tuner: the only displacement variable that change is *w* (the axial displacement), that now refers to the whole tuner, while the other displacements are always referred to half tuner (see Figure 34). In terms of forces, *Fx* and *Fz* are now applied to the whole tuner, while the torsion *Mz* is always applied to the half tuner. Therefore, considering a double axial stiffness due to the two half tuner and a double axial compliance due to the double length, the following relations are obtained:

$$\begin{Bmatrix} u_{LC} \\ w_{LR} \\ \psi_{LC} \end{Bmatrix} = 10^{-6} \begin{bmatrix} 66.537 & -0.7178 & 0.3098 \\ -1.4356 & 412.69 & 14.163 \\ 0.1549 & 3.5407 & 0.1246 \end{bmatrix} \begin{Bmatrix} Fx \\ Fz \\ Mz \end{Bmatrix}$$

which, by inversion, yields

$$\begin{Bmatrix} Fx \\ Fz \\ Mz \end{Bmatrix} = \begin{bmatrix} 20710 & 19427 & -2260193 \\ 38855 & 134950 & -15439000 \\ -1130096 & -3859750 & 449650000 \end{bmatrix} \begin{Bmatrix} u_{LC} \\ w_{LR} \\ \psi_{LC} \end{Bmatrix}$$

$$(\mathrm{N}, \mathrm{Nmm}) \qquad\qquad (\mathrm{mm}, \mathrm{rad})$$

or,

$$\begin{Bmatrix} u_{LC} \\ w_{LR} \\ Mz \end{Bmatrix} = 10^{-6} \begin{bmatrix} 66.17 & -9.526 & 2491 \cdot 10^3 \\ -19.07 & 10.155 & 113688 \cdot 10^3 \\ -1187 \cdot 10^3 & -28430 \cdot 10^3 & 8029340 \cdot 10^6 \end{bmatrix} \begin{Bmatrix} Fx \\ Fz \\ \psi_{LC} \end{Bmatrix}$$

The stiffness of the whole tuner has then been evaluated in three different boundary conditions, and the values obtained from the previous model are compared in Table 10 and Table 11.

5.5 Stiffness of whole tuner (including leverage)

The total stiffness of the tuner when equipped with the leverage mechanism can now be calculated. First of all we report the relation between the tuner and the leverage rotation:

$$\psi_{LC} \cong \theta \; d_2/r_e$$

From the principle of virtual work we can determine the relation between the torque on the tuner central ring and the torque applied at the leverage connection:

$$M_{Lev} \, \delta\theta = 4 \, M_z \, \delta\psi_{LC}$$

Remembering the stiffness of the leverage the following relation can be written:

$$M_z = \frac{M_{Lev}}{4} \frac{\delta\theta}{\delta\psi} \cong \frac{K_{Lev}}{4} \left(\frac{r_e}{d_2} \right)^2 \psi$$

Substituting the relation for M_z in the tuner stiffness we obtain:

$$\begin{Bmatrix} u_{LC} \\ w_{LR} \\ \psi_{LC} \end{Bmatrix} = \mathbf{C} \begin{Bmatrix} Fx \\ Fz \\ \dfrac{K_{Lev}}{4} \left(\dfrac{r_e}{d_2} \right)^2 \psi \end{Bmatrix} \rightarrow \begin{Bmatrix} u_{LC} \\ w_{LR} \end{Bmatrix} = \begin{bmatrix} C_{11} + C_{13} \dfrac{C_{31}}{1 - C_{33} \dfrac{K_{Lev}}{4} \left(\dfrac{r_e}{d_2} \right)^2} & C_{12} + C_{13} \dfrac{C_{32}}{1 - C_{33} \dfrac{K_{Lev}}{4} \left(\dfrac{r_e}{d_2} \right)^2} \\ C_{21} + C_{23} \dfrac{C_{31}}{1 - C_{33} \dfrac{K_{Lev}}{4} \left(\dfrac{r_e}{d_2} \right)^2} & C_{22} + C_{23} \dfrac{C_{32}}{1 - C_{33} \dfrac{K_{Lev}}{4} \left(\dfrac{r_e}{d_2} \right)^2} \end{bmatrix} \begin{Bmatrix} F_x \\ F_z \end{Bmatrix}$$

Note that the K_{Lev} used in the previous formula is not the same leverage stiffness computed in subsection 5.3.3, but:

$$K_{Lev} = \frac{2 d_2^2}{r_e^2} k_{mech} = 3.043 \cdot 10^7 \ \mathrm{Nmm}$$

By substituting the values of C_{ij}, K_{Lev} and $F_x = 0$, $F_z = 1$ the following displacement (or compliance because $F_z = 1$ N) has been obtained :

$$w_{LR} = 19.1 \ \mu\mathrm{m/kN}$$

Figure 35 shows the tuner compliance as a function of the stiffness of the leverage mechanism. A further increase of the leverage stiffness does not lead to a significant gain in the overall tuner stiffness.

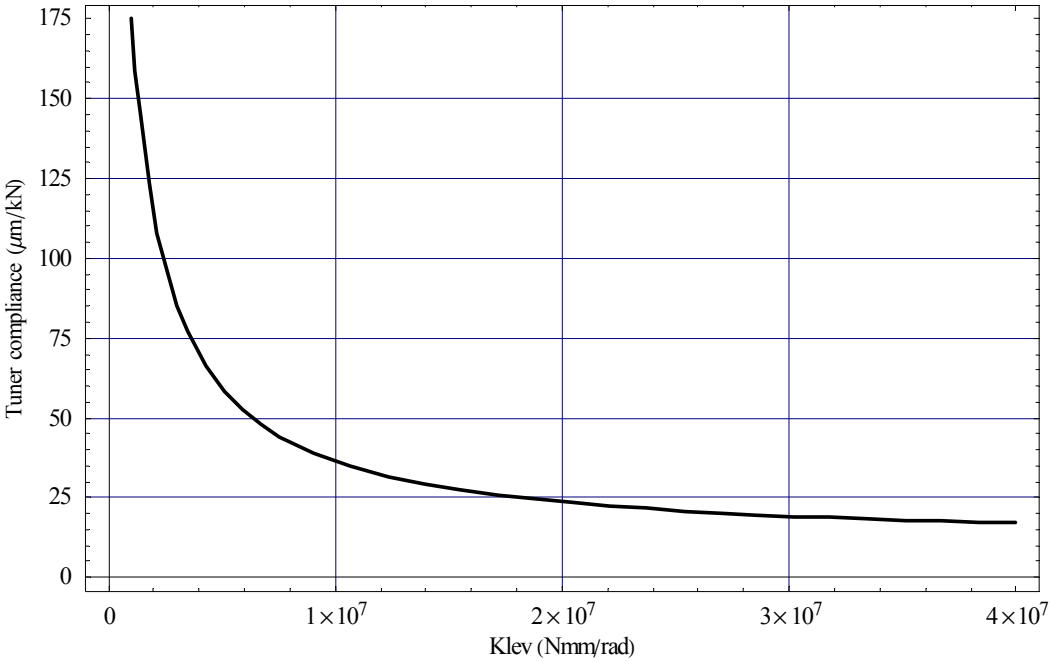

Figure 35. Tuner compliance as a function of the stiffness of the leverage mechanism.

Table 10: Tuner axial compliances for different boundary conditions (μm/kN).

Boundary conditions	2D model	3D model	3D model with leverage
Central ring can not rotate, but can translate in axial direction (ψ_{LC}=0, F_x=0)	---	10.1	19.1
Central ring can not rotate and translate (u_{LC} = 0, ψ_{LC}=0)	11.3	7.4	---
Central ring free (F_x=0, M_z=0)	718.5	412.7	---

Table 11: Tuner axial stiffness for different boundary conditions (kN/mm).

Boundary conditions	2D model	3D model	3D model with leverage
Central ring can not rotate, but can translate in axial direction (ψ_{LC}=0, F_x=0)	---	99.0	52.3
Central ring can not rotate and translate (u_{LC} = 0, ψ_{LC}=0)	88.5	135.1	---
Central ring free (F_x=0, M_z=0)	1.4	2.4	---

The values obtained by these analyses do not include the compliance of the motor and of the bearings. Moreover, the unavoidable lacks and slack joints can not be included consistently in the FE analysis, therefore it seems convenient to use as reference value for the total tuner stiffness the TTF tuner stiffness, which has been measured experimentally (25 kN/mm).In spite of the different geometries of the two tuners, the design has been scaled so to provide a similar stiffness. In fact the blade number is the same in both designs and the bigger dimensions of the leverage arm for the HIPPI case are compensated by the different saddles and plates adopted with respect to the TTF case.

6 Cavity equipped with Helium tank and Piezo Blade Tuner

The behavior of the cavity when equipped with the helium tank and the tuning system strongly depends from their stiffness. In this section axial and bending models are developed and commented out in order to evaluate the requirements for the piezo elements and check the compatibility with the technical specifications.

6.1 Mechanical characteristics

The mechanical characteristics of all components discussed in the previous paragraphs are summarized in the following table.

Table 12: Resume of mechanical characteristics of all parts

Part	Material	Axial stiffness	c (μm/kN)	k (kN/mm)	Notes
Helium tank	Ti Gr2	K_H	1.17	856	See 4.3.
Blade tuner (including leverage)	Ti Gr2/5	K_T	40.0	25	Experimental, from tests, see 5.5
Cavity	Nb	K_C	815.6	1.226	See 2.4.3.1
He tank dishes	Ti	K_W	63.4	15.7	Both dishes, see 3
Piezo actuator	PIC 255	K_P	4.76	2x105	L = 40 mm, from vendor
Tuner bellow	Ti Gr1	K_B	3205	0.312	See 4.4

6.2 Axial analysis

In this section a simplified model of the axial behavior, including all components in Table 12 is presented. With this model the displacements and forces corresponding to the slow and fast (piezo-based) tuning phases are evaluated.

6.2.1 Slow tuning

In the slow tuning phase the stepper motor applies deforms the blades in order to tune the cavity to the right frequency. Assume that the blade tuner applies a displacement δ_t to the system: in this case the cavity will be stretched and the helium tank compressed. Globally the system remains in equilibrium. The scheme in Figure 36 shows the axial stiffness model where K_{WH} is the helium tank and end dishes combined stiffness, and K_P, K_B and K_C are the stiffness of the piezo actuators, bellow and cavity, respectively.

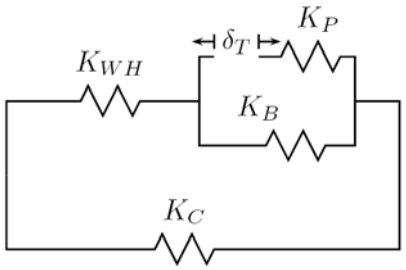

Figure 36: Axial model for the slow tuning action.

From simple considerations the expression of K_{WH} can be found:

$$K_{WH} = \frac{K_W K_H}{K_W + K_H} = 15.42 \text{ N}/\mu\text{m}$$

From equilibrium and congruence:

$$\begin{cases} \delta_C = \delta_T + \delta_{WH} + \delta_P \\ \delta_B = \delta_T + \delta_P \\ F_C = K_C \delta_C \\ F_{WH} = K_{WH} \delta_{WH} \\ F_P = K_P \delta_P \\ F_B = K_B \delta_B \\ F_{WH} = -F_C \\ F_{WH} = F_B + F_P \end{cases}$$

Solving the consistent equation it is possible to know the displacements of any part as a function of the tuner displacement:

$$\begin{cases} \Delta = K_P K_{WH} + K_B (K_C + K_{WH}) + K_C (K_P + K_{WH}) \\ F_P = -\dfrac{K_P [K_C K_{WH} + K_B (K_C + K_{WH})]}{\Delta} \delta_T \\ F_B = \dfrac{K_P K_B (K_C + K_{WH})}{\Delta} \delta_T \\ F_{WH} = -\dfrac{K_P K_C K_{WH}}{\Delta} \delta_T \\ F_C = \dfrac{K_P K_C K_{WH}}{\Delta} \delta_T \\ \delta_P = -\dfrac{K_C K_{WH} + K_B (K_C + K_{WH})}{\Delta} \delta_T \\ \delta_B = \dfrac{K_P (K_C + K_{WH})}{\Delta} \delta_T \\ \delta_{WH} = -\dfrac{K_P K_C}{\Delta} \delta_T \\ \delta_C = \dfrac{K_P K_{WH}}{\Delta} \delta_T \end{cases}$$

The axial forces that every part has to withstand for an imposed tuner displacement of 1 μm are reported in Table 13, while the displacements are reported in Table 14.

Table 13: Axial forces for a tuner displacement of 1 μm. Tensile forces are positive.

Part	Force for a δ_t = 1 μm (N)
Helium tank / End dishes	-1.128
Blade tuner	-1.438
Cavity	1.128
Piezo actuators (total force)	-1.438
Tuner bellow	0.310

Table 14: Axial displacements for a tuner displacement of 1 μm. Elongations are positive.

Part	Displacements for a δ_t = 1 μm (N)
Helium tank / End dishes	-0.073
Blade tuner	1
Cavity	0.920
Piezo actuators	-0.007
Tuner bellow	0.993

Thus, in the slow tuning action, 92% of the movement between the two lateral rings of the tuner is transferred to the cavity.

6.2.2 Fast tuning

In the fast tuning phase the piezo electric actuators move by some microns in order to contrast the Lorentz Force Detuning produced by the pulsed cavity operation. Assume that the piezo actuators apply a displacement δ_p to the system: in this case again the cavity will be stretched and the helium tank compressed. Dynamic effects here are not taken in account. Globally the system remains in equilibrium. The scheme in Figure 37 shows the axial stiffness model where K_{WH} is the helium tank and end dishes combined stiffness, and K_T, K_B and K_C are the stiffness of the complete tuner, bellow and cavity, respectively.

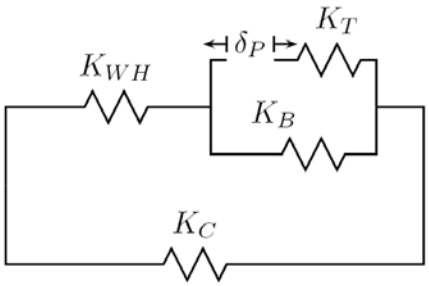

Figure 37: Axial model for the fast tuning action.

From equilibrium and congruence:

$$\begin{cases} \delta_C = \delta_T + \delta_{WH} + \delta_P \\ \delta_B = \delta_T + \delta_P \\ F_C = K_C \delta_C \\ F_{WH} = K_{WH} \delta_{WH} \\ F_T = K_T \delta_T \\ F_B = K_B \delta_B \\ F_{WH} = -F_C \\ F_{WH} = F_B + F_T \end{cases}$$

Solving the consistent equation it is possible to estimate the displacements of any part as a function of the piezo actuators displacement:

$$\begin{cases} \Delta = K_T K_{WH} + K_B\left(K_C + K_{WH}\right) + K_C\left(K_T + K_{WH}\right) \\ F_T = -\dfrac{K_T\left[K_C K_{WH} + K_B\left(K_C + K_{WH}\right)\right]}{\Delta}\delta_P \\ F_B = \dfrac{K_T K_B\left(K_C + K_{WH}\right)}{\Delta}\delta_P \\ F_{WH} = -\dfrac{K_T K_C K_{WH}}{\Delta}\delta_P \\ F_C = \dfrac{K_T K_C K_{WH}}{\Delta}\delta_P \\ \delta_P = -\dfrac{K_C K_{WH} + K_B\left(K_C + K_{WH}\right)}{\Delta}\delta_P \\ \delta_B = \dfrac{K_T\left(K_C + K_{WH}\right)}{\Delta}\delta_P \\ \delta_{WH} = -\dfrac{K_T K_C}{\Delta}\delta_P \\ \delta_C = \dfrac{K_T K_{WH}}{\Delta}\delta_P \end{cases}$$

The axial forces that every part has to withstand for a piezo displacement of 1 μm are reported in Table 15, while the displacement are reported in Table 16.

Table 15: Axial forces for a piezo displacement of 1 μm. Tensile forces are positive.

Part	Force for a δ_p = 1 μm (N)
Helium tank / End dishes	-1.073
Blade tuner	-1.368
Cavity	1.073
Piezo actuators (total force)	-1.368
Tuner bellow	0.295

Table 16: Axial displacements for a piezo displacement of 1 μm. Elongations are positive.

Part	Displacements for a δ_p = 1 μm
Helium tank / End dishes	-0.0696
Blade tuner	-0.0547
Cavity	0.8756
Piezo actuators	1
Tuner bellow	0.9453

In this case 87.6% of the piezo movement is transferred to the cavity for the LFD action.

6.3 Bending analysis of the cavity under dead load

In order to check the vertical displacements of the cavity and the stresses on the bellow under dead load, axisymmetric analyses with non axisymmetric load have been performed.

6.3.1 Cavity alone

This analysis is performed only for sake of comparison since the cavity is in this condition only during the manufacturing phase. The model used consists of 1762 shell elements and 1759 nodes (see Figure 38). The cavity is supported at the end dishes position.

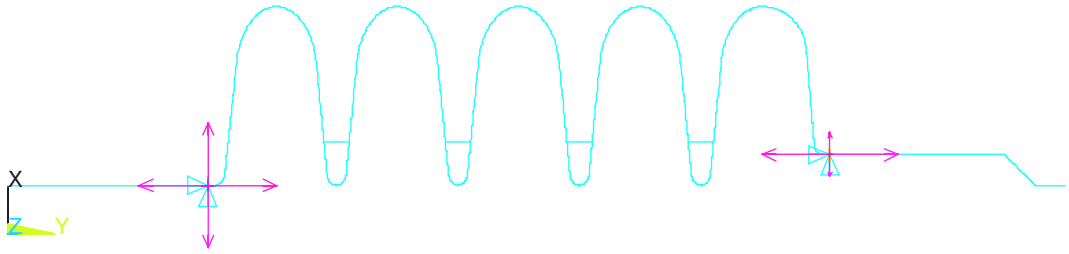

Figure 38: Axisymmetric model for the cavity under its dead load.

The total dead load is of 450 N and the maximum deflection calculated is equal to 0.14 mm (see Figure 39) for a maximum stress of 9 MPa.

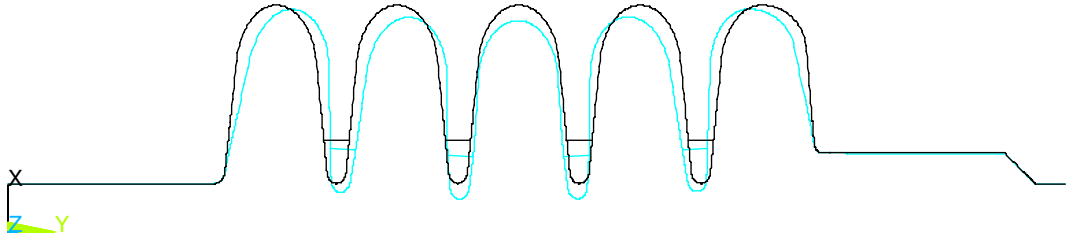

Figure 39: Vertical displacement of the cavity under its dead load (magnification factor = 200).

6.3.2 Cavity equipped with helium tank

This case represents the cavity before being equipped with the piezo blade tuner. The model used consists of 1900 shell elements and 1896 nodes (see Figure 42).The helium tank is supported by the support pads and several forces have been introduced in order to take in account the weight of the couplers and pick-up flanges.

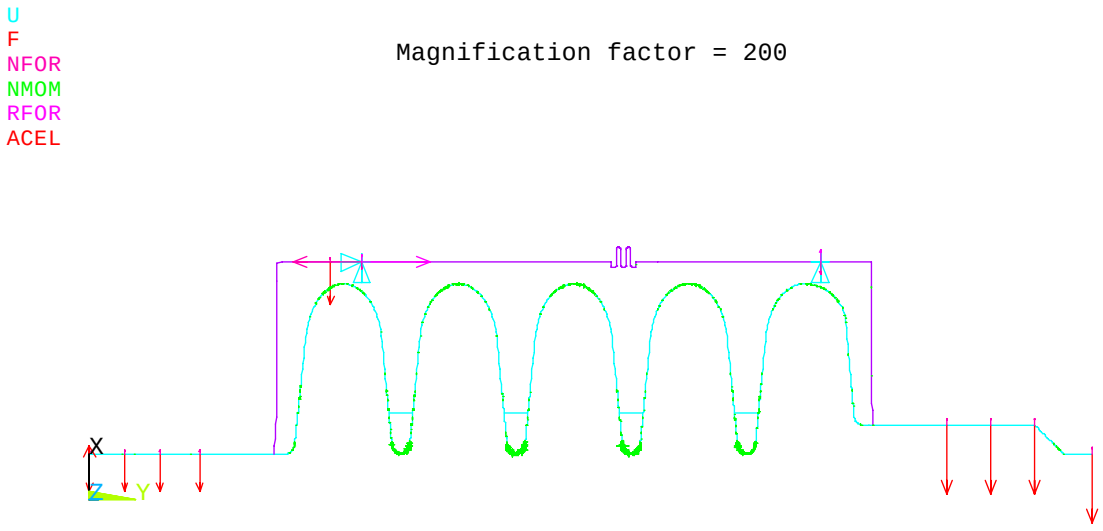

Figure 40: Axisymmetric model for the cavity equipped with the helium tank (dead load).

The total dead load is of 980 N and the maximum vertical displacement of the cavity is equal to 0.067 mm (see Figure 40) for a maximum stress of less than 6 MPa. The most important displacements are reported in Table 17.

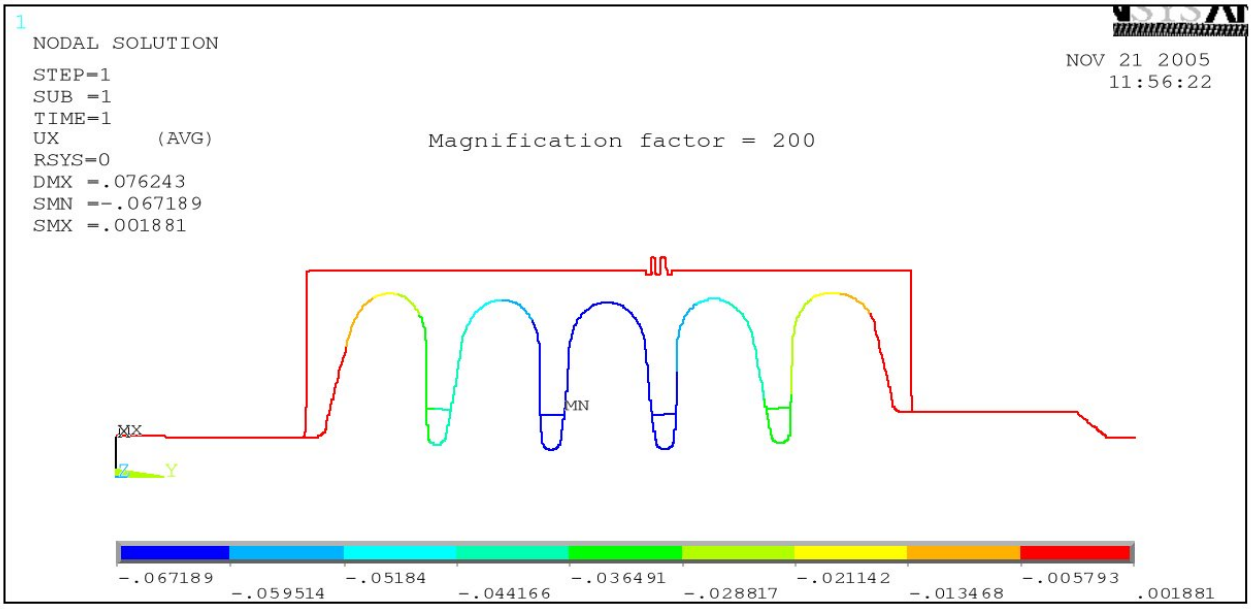

Figure 41: Vertical displacement of the cavity and helium tank (magnification factor = 200).

Table 17: Vertical displacements at the most important positions for cavity and helium tank.

Position	Helium tank displ. (mm)	Cavity displ. (mm)
Left end	-0.000	+0.002
Center	+0.000	-0.067
Right end	-0.001	-0.001
Maximum deflection	-0.001	-0.069

6.3.3 Cavity equipped with helium tank and piezo blade tuner

In the complete case the model consists of 1900 shell elements and 1896 nodes (see Figure 42), it accounts for only dead loads and neglects any possible vibration or external perturbation. It is important to point out that the tuner is considered only as a load and the stiffness effects due to the four existing stiffener bars are not considered.

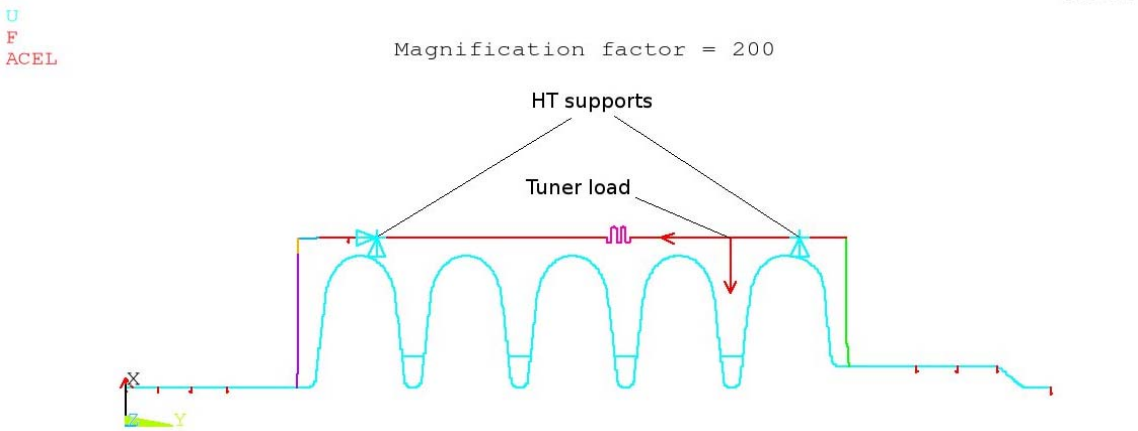

Figure 42: Axisymmetric model for the analysis of vertical displacements under dead load.

The total dead load (cavity plus helium tank and piezo blade tuner) is of 1240 N and the maximum vertical displacement of the cavity is of 0.071 mm at the center. Because the right end deflection is of 0.013 mm the maximum deflection of the cavity with respect to its ends is

of 0.071 + 0.013 = 0.084 mm, lower than the specifications required for the alignment of the cells. The most important displacements are reported in Table 18.

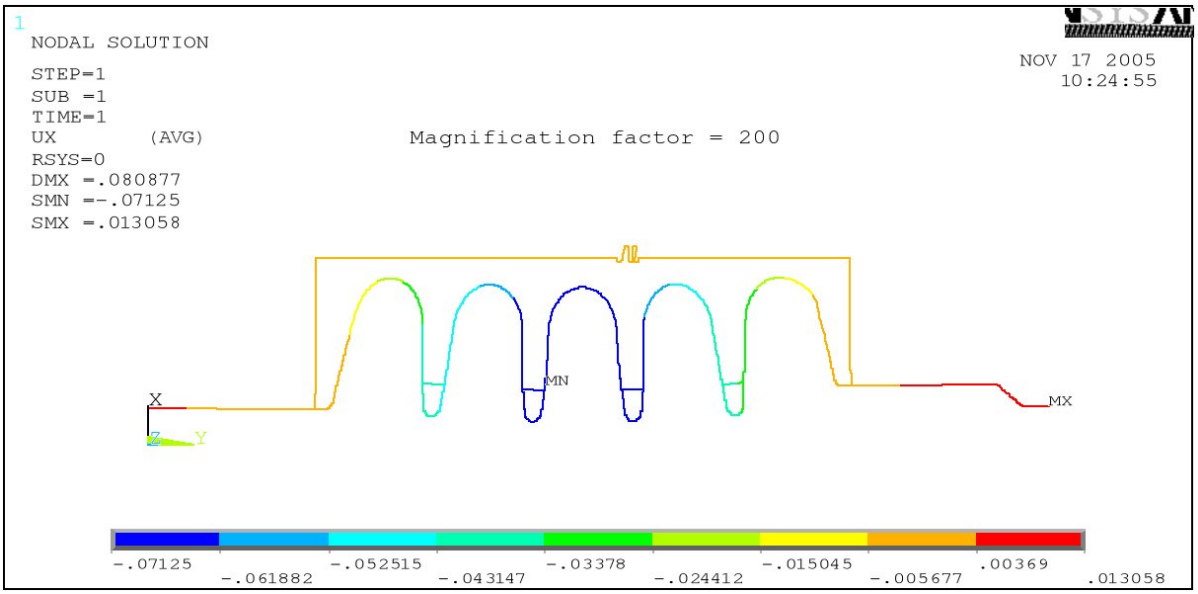

Figure 43: Vertical displacements due to the dead loads of the cavity, tank and tuner.

Table 18: Vertical displacements at the most important positions.

Position	Helium tank displ. (mm)	Cavity displ. (mm)
Left end	-0.000	+0.005
Center	-0.000	-0.071
Right end	+0.001	+0.013
Maximum deflection	-0.001	-0.084

7 Static Lorentz Force coefficient of the five cell structure

The behavior of the static Lorentz force coefficient for the full five cell structure is analyzed here, taking into account the influence of the boundary stiffness, i.e. the stiffness of the external support structure (which can be either the support frames for the vertical tests or the He tank and tuning system in a horizontal cryomodule).
The estimations obtained by the modeling will be then used in the paragraph 8 for the correct interpretation of the LFD coefficient measured during the vertical RF tests performed at Saclay and JLAB and reported in References [1] and [4].
The Lorentz force detuning is caused by the wall deformations arising from the pressures associated to the electromagnetic fields inside the RF structure, as discussed in paragraph 2.3.1.1. The pressure depends quadratically from the accelerating field excited in the cavity and acts outwards ("inflating" the cavity) in the region at the cell equators (dominated by the magnetic field) and inwards ("squeezing" the cavity) in the region at the cell irises (dominated by the electric field).
The pressure load, together with the applied boundary conditions, is used for the calculation of the cavity wall displacements, by performing a finite element analysis with ANSYS using the linear elastic material properties reported in Table 1.
First the case of a uniform cavity wall thickness of 4 mm is analyzed, and then the case for a thickness reduction at the equatorial weld is considered.
For an accelerating field of 10 MV/m the pressure acting on the cavity inner surface is displayed in the following figure. The color scale at the bottom of the figure is expressed in Pa (N/m^2). The pressure ranges from ~2.5 kPa (inward) at the irises to ~0.5 kPa at the equators (outward). The pressure load on the cavity walls has been obtained by the SEGFIELD postprocessor of the Superfish package.

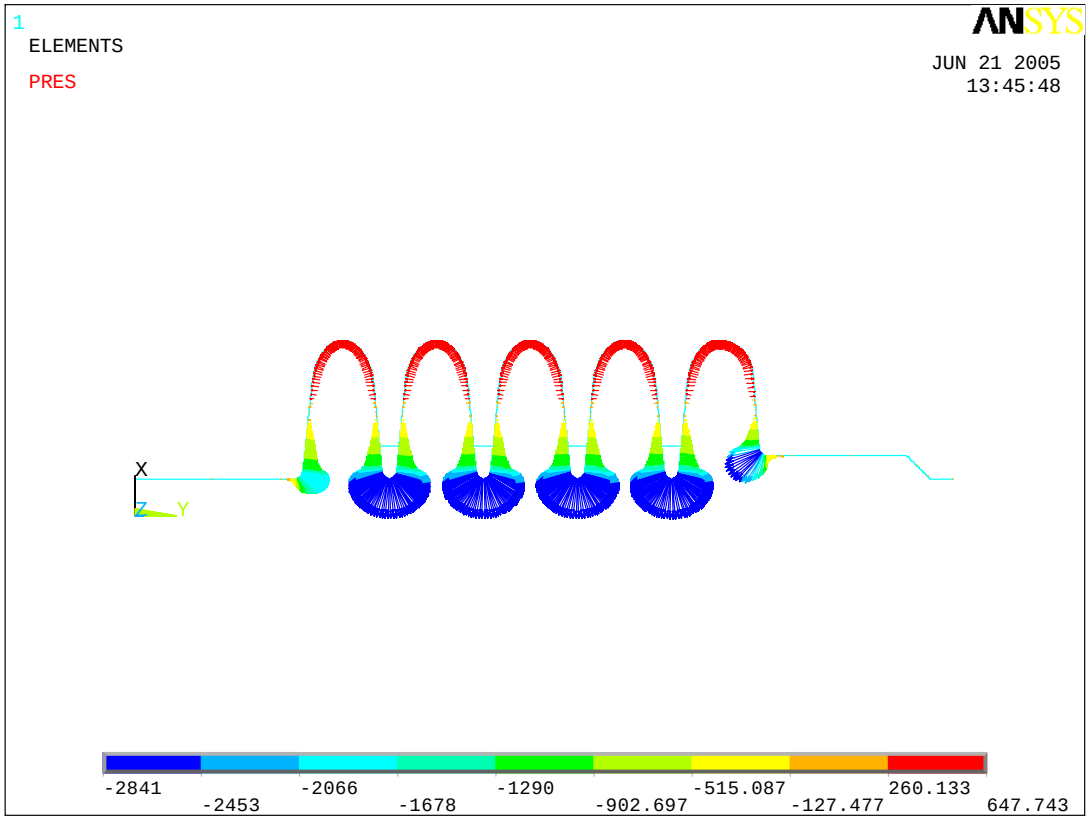

Figure 44: The static pressure on the cavity walls caused by an accelerating field of 10 MV/m.

7.1 Uniform thickness case

7.1.1 Infinitely rigid boundaries

Assuming an infinitely rigid boundary condition that maintains a fixed cavity length, the following displacement of the cavity shape is obtained (scaled by a factor of 10^5). The finite element model reports also the reaction force at the boundary, which is needed to maintain the fixed cavity length under the pressure load.

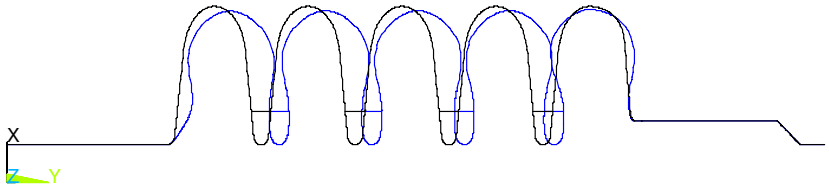

The wall displacements are then fed into the Slater procedure described in paragraph 2.3.1 in order to evaluate the frequency change and the ideal static Lorentz force detuning coefficient, and the results are summarized in Table 19.

Table 19: Full cavity static K_L^∞ (uniform thickness).

Frequency Displacement	-370.7 Hz
Reaction force at boundary, F^∞	-17.7 N
Accelerating field	10 MV/m
Static K_L^∞, with fixed boundary (SUPERFISH)	-3.70 Hz/(MV/m)^2
Static K_L^∞, with fixed boundary (SLATER)	-3.71 Hz/(MV/m)^2

7.1.2 Influence of the boundary stiffness

Similarly to the vacuum load case described in paragraph 2.4.3.2 the influence of the cavity support system can be assessed with the linear superposition of two effects. One is the frequency change induced by the geometrical displacement of the constrained cavity (deformation of the shape of the cavity), and the other is the frequency offset caused by the cavity shortening driven by the longitudinal component of the overall pressure load at the cavity constraint ($-F^\infty$), acting on the combined system with the external stiffnes K_{ext} in series with the cavity spring coefficient K_{cav}. In short:

$$K_L = K_L^\infty + \frac{\partial f}{\partial z}\frac{F^\infty / E_{acc}^2}{K_{ext} + K_{cav}}$$

The behavior of the K_L as a function of the external stiffness K_{ext}, using the parameters of Table 2 and Table 19, is shown by the red line in Figure 45.
This simple model has been checked for validity with ANSYS computations using an external stiffening system characterized by K_{ext}. As it can be seen, the ANSYS simulations (blue squares) performed with a finite stiffness of the external cavity support agrees perfectly with the analytical estimation (red curve) that can be obtained from the ideal infinitely stiff boundary simulation and from the cavity tuning coefficient.
Figure 46 shows the geometry (and pressure loads) used in ANSYS to take into account a "soft" external cavity stiffening system. A stiffening tube of a given length and cross sectional area has been employed in the model, one end of which has been coupled in the longitudinal DOF with the cavity He Tank position. The support stiffness was then parametrically changed by varying the material Young modulus E_x, with the relation:

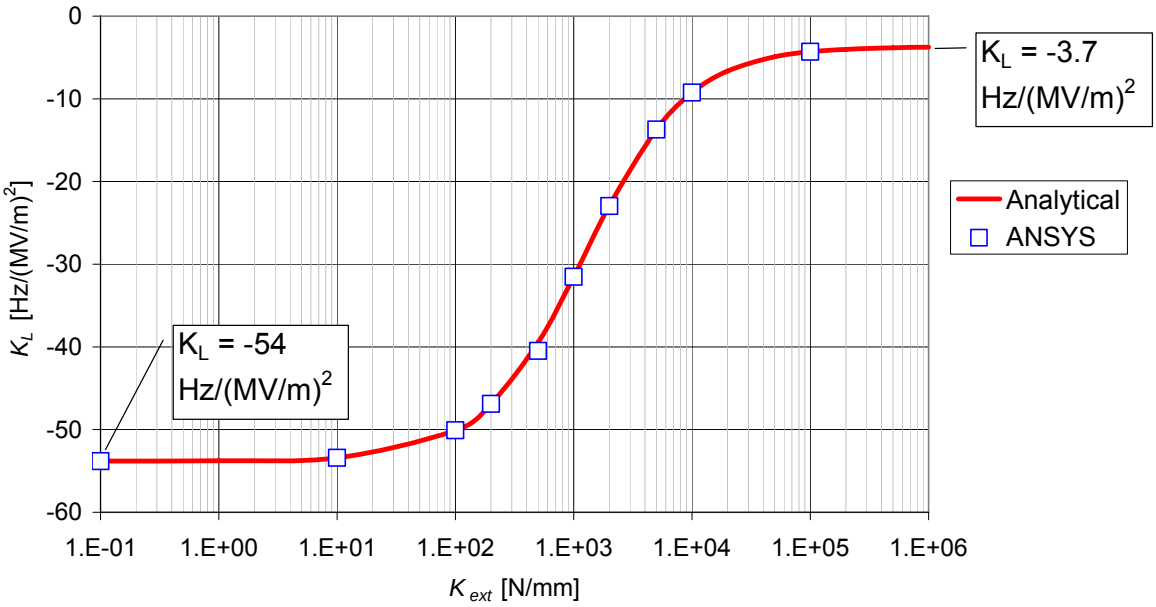

Figure 45: Static LFD coefficient as a function of the boundary stiffness.

$$K_{ext} = E_x \frac{2\pi R\, h}{L}$$

Where R is the tube radius, h its thickness and L the length.
The results obtained by this model by varying the external stiffening with the material E_x agree perfectly with the simple analytical model described above, as it can be seen from the Figure 45, where the ANSYS results are identified by the blue squares.

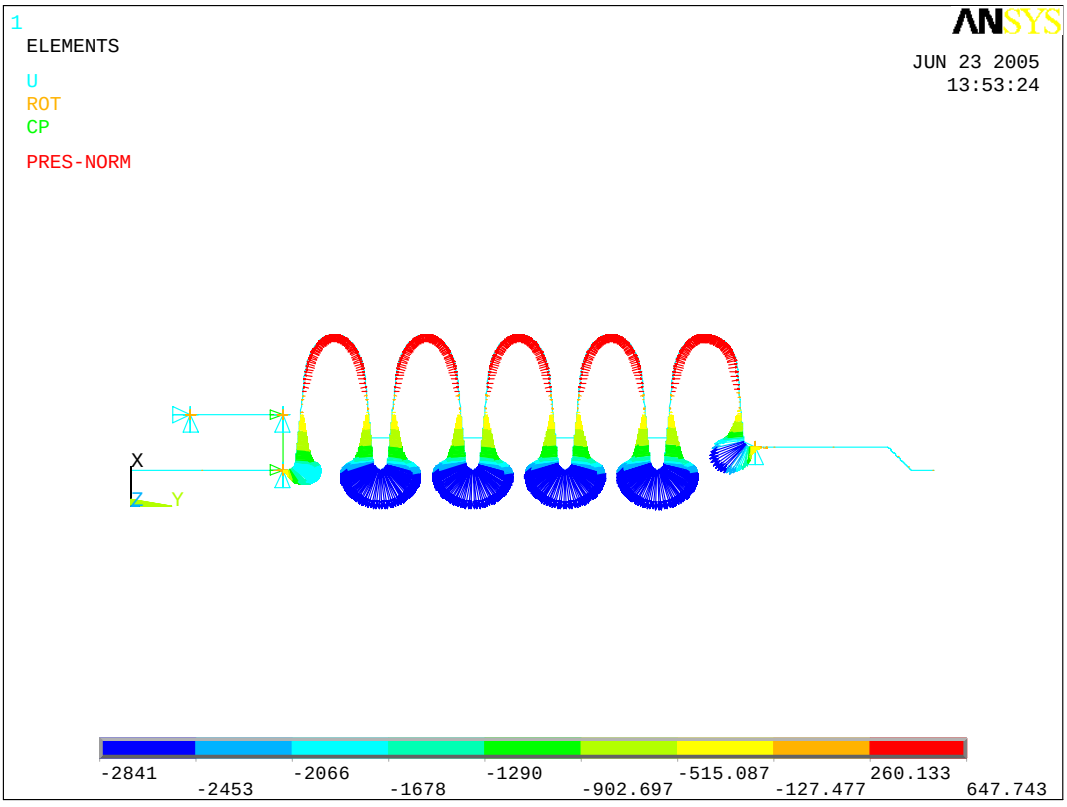

Figure 46: ANSYS model to simulate an arbitrary external boundary stiffness.

7.2 Equatorial weld reduction

The case of the model with the reduced equatorial weld described in paragraph 2.4.4 is considered here. First the cavity is characterized with infinitely rigid boundaries, and then the influence of the boundary stiffness will be discussed with the analytical model, using the cavity spring and frequency sensitivity coefficients reported in 2.4.4.1.
Since the calculation procedure has been extensively discussed in the previous paragraph, only the tabular results are presented in the following discussion.

7.2.1 Infinitely rigid boundaries

The results of the 10 MV/m pressure load case are reported in Table 20. These values, together with the values listed in Table 4.

Table 20: Full cavity static K_L^{∞} (reduced equatorial weld).

Static K_L^{∞}, with fixed boundary (SLATER)	-4.44 Hz/(MV/m)^2
Reaction force at boundary, F^{∞}	-17.5 N

7.2.2 Influence of the boundary stiffness

The effect of the boundary stiffness on the K_L is shown below (in terms of its absolute value) and compared to the previous case of uniform Nb thickness. The curves are plotted on a double logarithmic scale in order to perceive the small difference that can be seen approaching the infinitely rigid case. For a weak boundary condition (<10^4 N/mm) the detuning effect due to the change in the cavity length is dominant with respect to the contribution of the shape deformation, and hence the prediction given by the two models cannot be appreciated. Only approaching a stiff boundary condition, the model that accounts for the equatorial weld reduction predicts a 20% higher LFD coefficient.

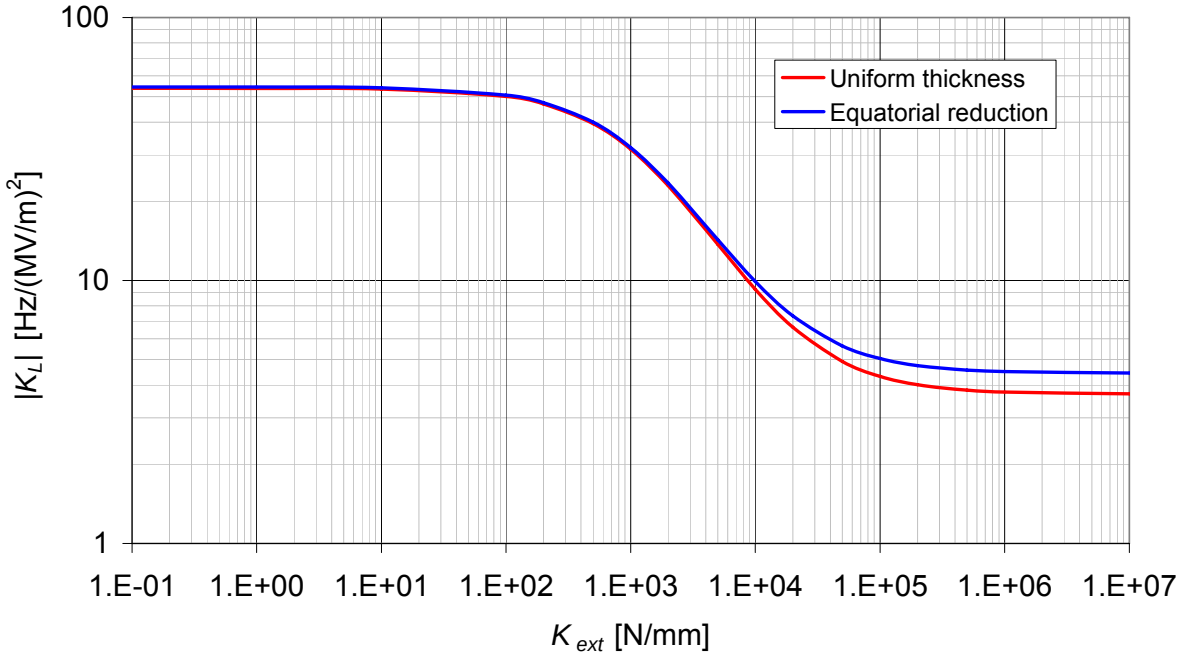

Figure 47: Comparison between the static LFD coefficient of the two models.

7.3 LFD measurements during tests at JLAB and Saclay

The static K_L has been tested both at JLAB and Saclay [4], with a relative large spread in the results. The measurements have been reported at EPAC 2004, and are summarized here.
At CEA/Saclay the three consecutive RF measurements yielded a LFD K_L value in the range from -20 to -32 Hz/(MV/m)^2, whereas the three RF measurements at JLAB (the cavity has been disassembled and reassembled in the vertical insert of the cryostat between the three tests) gave -47, -24 and -31 Hz/(MV/m)^2, respectively.
On the basis of the K_L characterization of the cavity outlined in the preceding paragraphs, the RF measurement can be interpreted correctly is the stiffness of the vertical inserts is:

- lower than 1.5 kN/mm (<1.5 10^6 N/m) for the JLAB case
- in the range between 1 and 2.6 kN/mm (1÷2.6 10^6 N/m) for the Saclay case.

In both cases the stiffness of the structure seems to be comparable to the cavity stiffness (1.2 kN/mm). In the following paragraph all details concerning the experimental inserts are gathered and the characteristics of the two support structures used in these measurements are analyzed and correlated with the measured K_L coefficients.

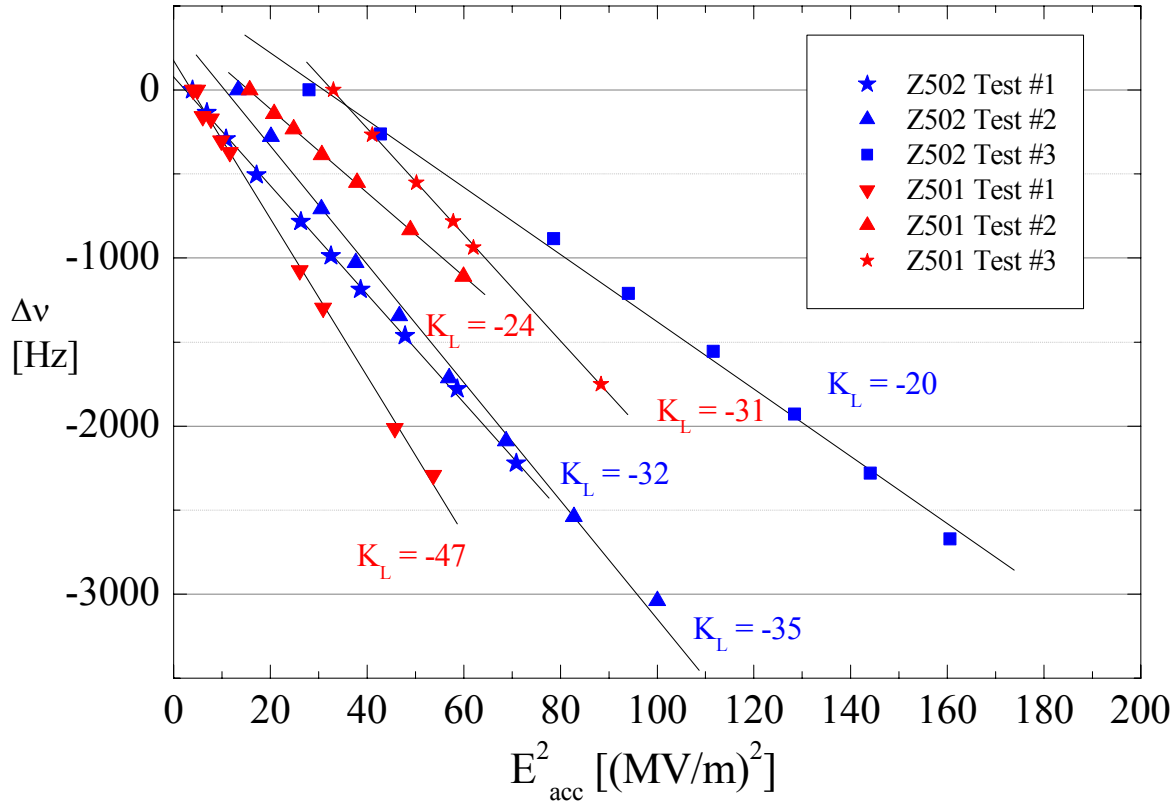

Figure 48: Frequency deviation and LFD coefficients for the Saclay and JLAB tests.

7.4 External stiffness under operating conditions

From the values reported in Table 12 it is possible to obtain the external stiffness seen from the cavity under operating condition with the piezo blade tuner. Considering that the Helium tank and the end dishes are in series with the tuner and the piezo elements (and neglecting the modest contribution of the bellow, which is in parallel with these elements), the external stiffness is easily obtained:

$$\frac{1}{k_{bc}} = \frac{1}{k_{WH}} + \frac{1}{k_T} + \frac{1}{k_P} \Rightarrow k_{bc} = 9.1 \text{ (kN/mm)}$$

This value corresponds in Figure 47 to a K_L in the range of -10 Hz/(MV/m)^2.

8 Interpretation of the vertical tests at JLAB and Saclay

In this section all available data from the vertical frames is collected and the corresponding stiffness is assessed for the correct interpretation of the LFD coeeficient derived from the RF measurements presented in paragraph 7.3.

8.1 Analysis of the JLAB test conditions

The JLAB insert is the cavity handling cage used for the SNS cavities characterization, slightly modified for the different geometry of the TRASCO cavity. A paper at SRF2001 [8] reports the original SNS frame stiffness at 5.33 kN/mm, which would correspond to a LFD K_L = -14 Hz/(MV/m)^2. All technical information concerning the insert has been retrieved from JLAB. Figure 49 shows the CAD model of the 16"x16", followed by a picture showing the adaptations to the TRASCO cavity for the tests.

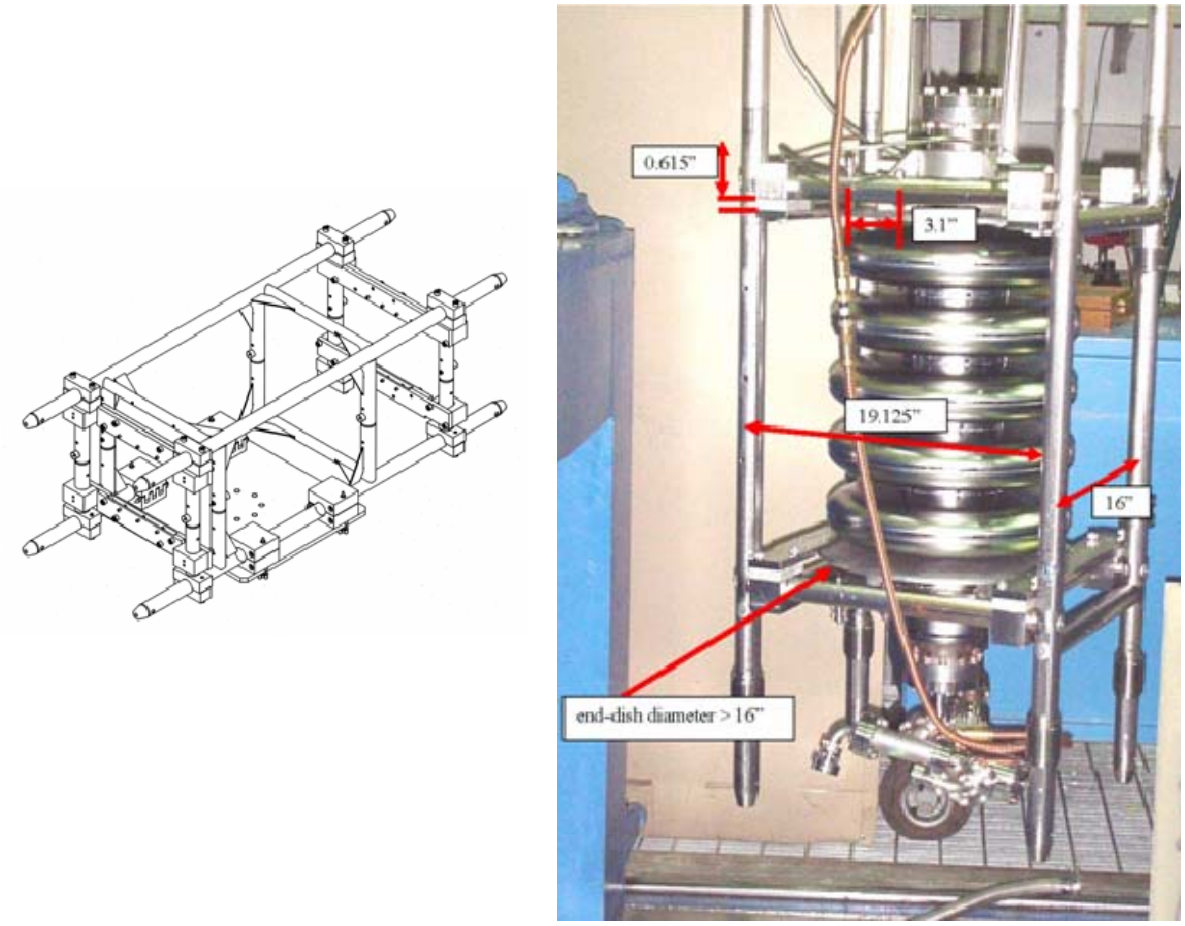

Figure 49: The JLAB insert for the vertical tests.

The axial stiffness of the four Ti rods can be computed easily (outer diameter of 1.5", thickness of 0.065", for a length of 22"), leading to a K_{rods} = 142 kN/mm.
The limiting factor that does not allow to achieve this high axial stiffness is given by the two supports that connect to the end dishes, and by the end dishes stiffness itself. The supports have been modeled in order to determine their axial stiffness, and the output of a forced displacement of 1 mm at the cavity connection is shown below, yielding a reaction force of 13 kN. From this analysis and the complementary load case of a force loading of 1000 N, an average support system stiffness of ~ 11 kN/mm has been evaluated.

The frame stiffness thus can be evaluated by the series connection of the two systems (the rods and the two supports), yielding an "ideal" stiffness (neglecting the connections) of K_{frame} = 10.2 kN/mm. The result of the support simulation is shown in Figure 50.

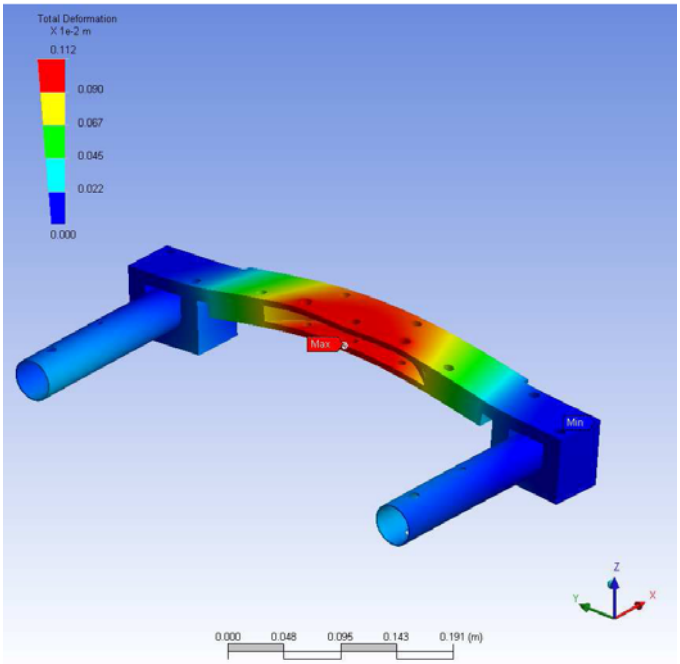

Figure 50: Support that holds the end dishes to constrain the cavity length.

However, since the support shown in the above picture acts on the end dishes, the stiffness of the whole system, from the point of view of the constraint provided to the cavity length, is greatly reduced:

$$\frac{1}{K_{jlab}} = \frac{1}{K_{frame}} + \frac{1}{K_{Dbig}} + \frac{1}{K_{Dsmall}} \Rightarrow K_{jlab} = 0.93\,\text{kN/mm}$$

This result is in good agreement with the large K_L experienced in the JLAB tests. The results of the analysis are summarized in Table 21.

Table 21: Summary of the JLab support analysis

Frame contributions	
Ti rods	142 kN/mm
Supports	11 kN/mm
End dish contribution	
Large dish	2.1 kN/mm
Small dish	2 kN/mm
Total K_{ext} seen by the cavity	
K_{ext}	0.93 kN/mm
Expected Lorentz Force Detuning	
K_L	-33 Hz/(MV/m)^2
Average test result	
Average(-47,-24, -31)	-34 Hz/(MV/m)^2

8.2 Analysis of the Saclay tests conditions

The Saclay frame for the vertical test is even simpler in concept, and is displayed in the picture shown below. It is composed of three stainless steel rods with a diameter of 12 mm, connected to a star-shaped support, at 275 mm from the cavity axis. The connecting arms are 60 mm wide and the plate thickness is 20 mm.

Figure 51: The cavity under assembly in Saclay.

A model of the above system has been created in ANSYS and its stiffness has been evaluated to be 2.8 kN/mm (using a stainless steel Young modulus of 200 GPa). All part contacts are assumed to be rigid and initial adjustments or deformations have been ignored, thus providing an optimistic estimate of the frame stiffness.
Figure 52 shows the load condition, with an imposed displacement of 1 mm at the cavity end flange and the deformed shape of the support, which develops a reaction force of ~2.5 kN at the constraint. This solution, together with the reciprocal solution of an applied load of 1 kN, which yields a longitudinal displacement of 0.444 mm, results in an average estimation of 2.4 kN/mm for the Saclay stiffening system (which was estimated in the range 1-2.6 kN/mm from the RF measurement). The results are summarized in Table 22.
Thus, also the K_L measured at Saclay is in good agreement with the expected frame stiffness, since it is around .-21 Hz/(MV/m)^2 for the both uniform thickness and reduced welds cases.

Table 22: Summary of the Saclay support analysis.

Displacement load condition	
δz	1 mm
Reaction force	2.536 kN
Force load condition	
Applied force	1.000 kN
Max δz	0.444 mm
Average frame stiffness	
k_{frame}	2.39 kN/mm
Expected Lorentz Force Detuning	
K_L	-21 Hz/(MV/m)^2
Average test result	
Average (-20,-32,-35)	-29 Hz/(MV/m)^2

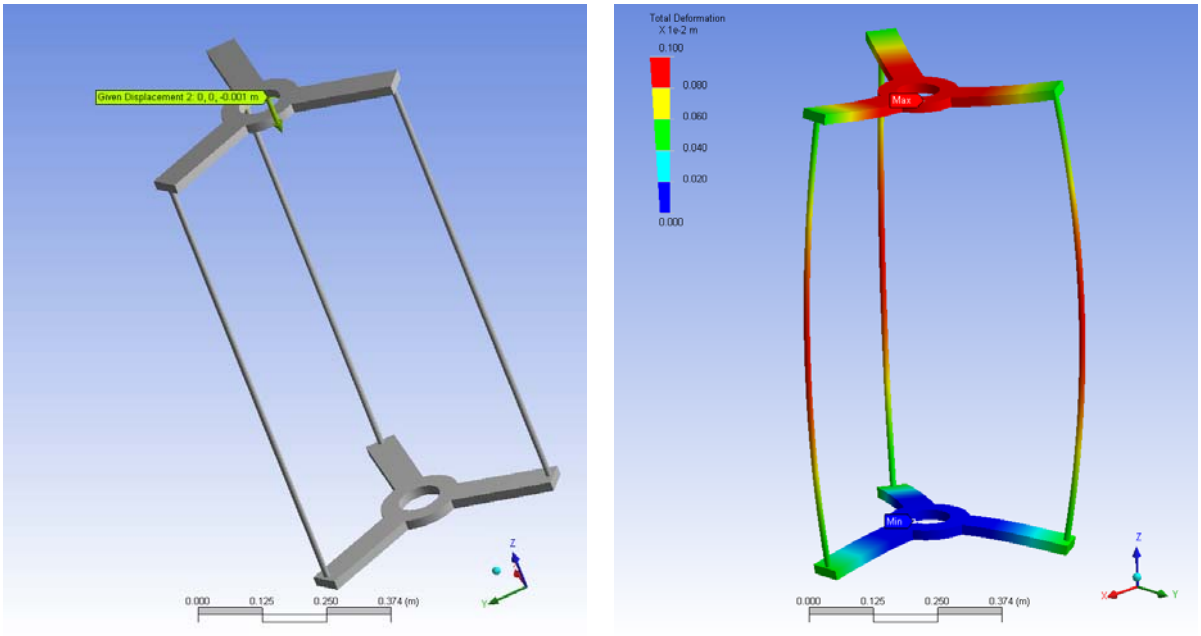

Figure 52: ANSYS modeling of the Saclay vertical insert for the tests.

8.3 Conclusions of the RF tests interpretation

Finally, the results of both tests are displayed below together with the cavity K_L characterization shown in the previous section. A much stiffer cavity constraint needs to be experimentally realized for such a weak cavity in order to reach its "ideal" behavior.

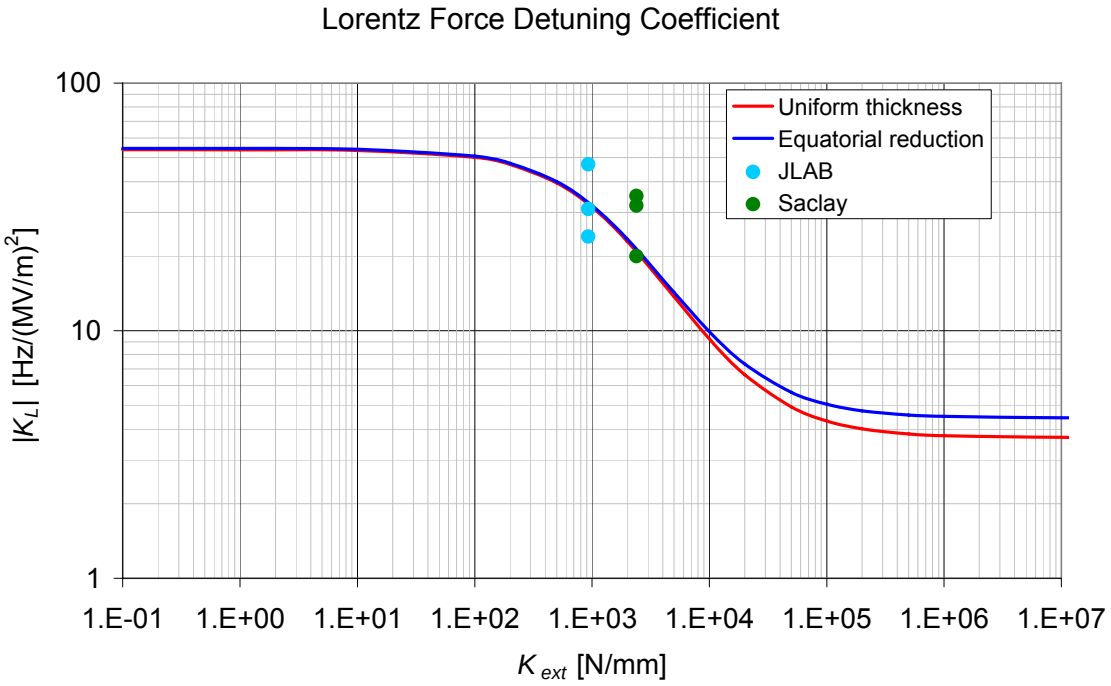

Figure 53: Comparison of the Saclay and JLAB measurements with the model estimations.

8.4 Alternative characterization of the support stiffness

An independent method can be used [10] to estimate the effective support system stiffness employed in the measurements, by looking the frequency dependence at low RF power from the test temperature (the data is generally taken to characterize the residual resistance of the niobium material). This data can be transformed in a behavior of the frequency shift against the He bath pressure and interpreted with the pressure analysis load case shown in the paragraph 2.4.3.2.

From the Saclay data at low temperatures (2.2 to 1.7 K, where the bath pressure is more stable), an average value of $\Delta\nu/\Delta P$ of -462 Hz/mbar can be evaluated. Using the model and coefficient discussed in the previous paragraphs, a K_{ext} of 1.15 kN/mm can be estimated, within the range suggested by the interpretation of the K_L results.

From the JLab data an average of $\Delta\nu/\Delta P$ of -1020 Hz/mbar in the same temperature range can be estimated. This is comparable to a “free” cavity behavior (nominal -966 Hz/mbar), with a negligible external stiffness condition with respect to the cavity stiffness.

9 Cavity mechanical eigenmodes

Using the structural model developed in the previous sections, we have found 63 structural eigenmodes in the range from 10 Hz to 10 kHz. Their frequencies are listed in the following table.

Table 23: Frequency of the structural eigenmodes of the cavity.

Mode	f [Hz]	Mode	f [Hz]	Mode	f [Hz]	Mode	f [Hz]
1	81.275	**21**	2680.3	**41**	5818.1	**61**	9559.1
2	161.17	**22**	2729.4	**42**	5836.6	**62**	9709.0
3	237.71	**23**	2784.6	**43**	5901.4	**63**	9802.9
4	305.94	**24**	2850.1	**44**	5911.9		
5	351.20	**25**	3118.5	**45**	6092.6		
6	537.11	**26**	3339.9	**46**	6235.3		
7	593.81	**27**	3447.2	**47**	6264.2		
8	650.62	**28**	3599.8	**48**	6295.2		
9	693.28	**29**	3773.6	**49**	6330.9		
10	1036.8	**30**	3951.2	**50**	6542.9		
11	1235.3	**31**	4171.6	**51**	6942.0		
12	1328.8	**32**	4372.7	**52**	7114.5		
13	1376.2	**33**	4572.8	**53**	7331.2		
14	1426.6	**34**	4755.2	**54**	7535.9		
15	1585.5	**35**	5057.0	**55**	8145.6		
16	1669.2	**36**	5377.3	**56**	8454.1		
17	1805.3	**37**	5447.2	**57**	8643.6		
18	1833.6	**38**	5544.9	**58**	8882.0		
19	1855.6	**39**	5714.4	**59**	9123.0		
20	2276.4	**40**	5773.9	**60**	9391.7		

Given the modal displacement pattern, the corresponding static frequency shifts could be evaluated through the nodal displacements by using the same procedure described in the preceding sections. This procedure is useful for the evaluation of dynamic LFD effects.

10 Conclusions

In this note we have reported the RF and mechanical characterization of the TRASCO cavity (Cavity A in HIPPI) and its tuner, developed as part of the HIPPI work program.
The tuner has been characterized in terms of its capabilities of slow and fast tuning action.
In terms of slow tuning range capabilities, the tuner, with the present configuration of the leverage mechanism allowing a 1.3 mm excursion, can compensate a maximum cavity detuning given by:

$$\Delta\nu_{slow} = 1.3\,\text{mm} \cdot 350\,\text{kHz/mm} \cdot 92\% \approx 420\,\text{kHz}$$

And, if needed, with minimal modification to the leverage mechanism, this value can be approximately doubled.
For the pulsed operation foreseen by the HIPPI specifications, one of the major uncertainties is still given by the stroke capabilities of the piezo under the 2 K operating conditions, which is still under investigation of the CARE-JRA1-WP8. According to the latest work of this work package, piezo elements with the correct length seems capable to provide at least a 3 μm stroke at 2 K. Their action would be then able to compensate a frequency offset given by:

$$\Delta\nu_{p} = 3\,\mu\text{m} \cdot 350\,\text{Hz/}\mu\text{z} \cdot 87.6\% \approx 920\,\text{Hz}$$

Thus, the Lorentz Force Detuning should be limited to this value (with some margin to account for dynamic effects), and, at the design gradient of 7 MV/m of the HIPPI specifications, this results in a requirement for the LFD coefficient K_L given by:

$$K_L > -\frac{\Delta\nu_p}{E_{acc}^2} = -\frac{920}{49} = -18.8\ \text{Hz/(MV/m)}^2$$

This condition is fulfilled it the external stiffness provided to the cavity is greater than 3 kN/mm. In paragraph 7.4 the stiffness provided to the cavity under operating conditions was estimated to be greater than 9 kN/mm, assuming a conservative value for the tuner system (25 kN/mm, nearly half of the value resulting from the FEM analyses). This value accounts for the tuner structure, leverage mechanism, end dishes and piezo elements.
We are therefore confident that the tuner under construction will be able to demonstrate pulsed operation capabilities of the TRASCO Cavity A during horizontal tests at high RF power, as required by the HIPPI program.

11 Acknowledgements

We acknowledge the staff at ZANON and INFN Milano LASA for their work on the beta 0.47 structures, and the work of our colleagues at CEA/Saclay and JLAB for the RF measurements. We acknowledge also the support of the European Community-Research Infrastructure Activity under the FP6 "Structuring the European Research Area" programme (CARE, contract number RII3-CT-2003-506395).

12 References

[1] A. Bosotti, C. Pagani, P. Pierini, P. Michelato, R. Paulon, G. Corniani, J. P. Charrier, B. Visentin, Y. Gasser, J. P. Poupeau, B. Coadou,, REPORT ON CAVITY A (TRASCO Z502) FABRICATION AND TESTS, **CARE-NOTE-2005-001-HIPPI**.

[2] D. Barni, A. Bosotti, G. Ciovati, C. Pagani, P. Pierini, "SC CAVITY DESIGN FOR THE 700 MHZ TRASCO LINAC", in *Proceedings of EPAC 2000*, Vienna, Austria, p. 2019.

[3] D. Barni, A. Bosotti, C. Pagani, R. Paulon, P. Pierini, H. Safa, G. Ciovati, P. Kneisel, "RF TESTS OF THE SINGLE CELL PROTOTYPES FOR THE TRASCO B=0.47 CAVITIES", in *Proceedings of EPAC2002*, Paris, France, p. 2277.

[4] A. Bosotti, C. Pagani, P. Pierini, J.P. Charrier, B. Visentin, G. Ciovati, P. Kneisel, "RF TESTS OF THE BETA=0.5 FIVE CELL TRASCO CAVITIES", in *Proceedings of EPAC 2004*, Lucerne, Switzerland, p. 1024.

[5] E. Haebel J. Tuckmantel, "ELECTROMAGNETIC SURFACE FORCES IN RF CAVITIES", CERN-AT-RF(Int)-91-99, 11 December 1991.

[6] D. Barni, A. Bosotti, C. Pagani, "A NEW TUNER FOR TESLA", in *Proceedings of EPAC 2002*, Paris, France, p. 2205.

[7] J. Sekutowicz et al., "TEST OF TWO NB SUPERSTRUCTURE PROTOTYPES", in *Phys. Rev. ST-AB*, **7**, 012002 (2004).

[8] C. Pagani, A. Bosotti, P. Michelato, R. Paparella, N. Panzeri, P. Pierini, F. Puricelli, G. Corniani,, "REPORT ON FAST PIEZO BLADE TUNER (UMI TUNER) FOR SCRF RESONATORS DESIGN AND FABRICATION", **CARE-NOTE-2005-021-SRF**.

[9] R. Mitchell, K. Matsumoto, G. Ciovati, K. Davis, K. Macha, R. Sundelin, "LORENTZ FORCE DETUNING ANALYSIS OF THE SPALLATION NEUTRON SOURCE (SNS) ACCELERATING CAVITIES"; in *Proceedings of the SRF2001 Workshop*, Tsukuba, Japan.

[10] G. Devanz, private communication.